NASA TECHNICAL REPORT

NASA TR R-450

DEVELOPMENT AND DEMONSTRATION OF A FLUTTER-SUPPRESSION SYSTEM USING ACTIVE CONTROLS

Maynard C. Sandford, Irving Abel, and David L. Gray

Langley Research Center
Hampton, Va. 23665

NATIONAL AERONAUTICS AND SPACE ADMINISTRATION • WASHINGTON, D. C. • DECEMBER 1975

1. Report No.	2. Government Accession No.	3. Recipient's Catalog No.
NASA TR R-450		

4. Title and Subtitle	5. Report Date
DEVELOPMENT AND DEMONSTRATION OF A FLUTTER-SUPPRESSION SYSTEM USING ACTIVE CONTROLS	December 1975
	6. Performing Organization Code
7. Author(s)	8. Performing Organization Report No.
Maynard C. Sandford, Irving Abel, and David L. Gray	L-10446
	10. Work Unit No.
9. Performing Organization Name and Address	743-05-04-01
NASA Langley Research Center Hampton, Va. 23665	11. Contract or Grant No.
	13. Type of Report and Period Covered
12. Sponsoring Agency Name and Address	Technical Report
National Aeronautics and Space Administration Washington, D.C. 20546	14. Sponsoring Agency Code

15 Supplementary Notes

16. Abstract

The application of active control technology to suppress flutter has been demonstrated successfully in the Langley transonic dynamics tunnel with a delta-wing model. The model was a simplified version of a proposed supersonic transport wing design. An active flutter-suppression method based on an aerodynamic energy criterion has been verified by using three different control laws. The first two control laws utilized both leading-edge and trailing-edge active control surfaces, whereas the third control law required only a single trailing-edge active control surface. At a Mach number of 0.9 the experimental results demonstrated increases in the flutter dynamic pressure from 12.5 percent to 30 percent with active controls. Analytical methods were developed to predict both open-loop and closed-loop stability, and the results agreed reasonably well with the experimental results.

17. Key Words (Suggested by Author(s))	18. Distribution Statement
Flutter Active controls Flutter suppression	Unclassified – Unlimited Subject Category 39

19. Security Classif. (of this report)	20. Security Classif. (of this page)	21. No. of Pages	22. Price*
Unclassified	Unclassified	67	$4.25

*For sale by the National Technical Information Service, Springfield, Virginia 22161

CONTENTS

DEVELOPMENT AND DEMONSTRATION OF A FLUTTER-SUPPRESSION SYSTEM USING ACTIVE CONTROLS

Maynard C. Sandford, Irving Abel,
and David L. Gray
Langley Research Center

SUMMARY

The application of active control technology to suppress flutter has been demonstrated successfully in the Langley transonic dynamics tunnel with a delta-wing model. The model was a simplified version of a proposed supersonic transport wing design. An active flutter-suppression method based on an aerodynamic energy criterion has been verified by using three different control laws. The first two control laws utilized both leading-edge and trailing-edge active control surfaces, whereas the third control law required only a single trailing-edge active control surface. At a Mach number of 0.9 the experimental results demonstrated increases in the flutter dynamic pressure from 12.5 percent to 30 percent with active controls. Analytical methods were developed to predict both open-loop and closed-loop stability, and the results agreed reasonably well with the experimental results.

INTRODUCTION

Flutter is a hazardous oscillatory phenomenon which has plagued aircraft designers since the early days of manned flight. An excellent historical review of the development of flutter technology is presented in reference 1 which cites papers on flutter as early as 1916. Since that time, the development of flutter technology has relied exclusively on passive flutter control methods, such as adding structural stiffness, mass balance, damping mechanisms and, in some cases, changing the geometry. Passive flutter control in most cases results in undesirable increased cost and decreased performance of the subject aircraft. These considerations along with modern aircraft design trends toward increased flexibility and higher operating speeds have refocused attention on the flutter problem and emphasized the need for more efficient approaches to flutter prevention. Recent advances in active control technology offer a new and promising approach to the flutter control problem. The subject of this report focuses on a new approach known as active flutter suppression. Active flutter suppression is the prevention of flutter by utilizing a controllable

force (that is, an aerodynamic control surface) which responds in a predetermined manner (control law) to feedback signals from motion sensors located on the main lifting surface.

Two decades ago published reports (refs. 2 and 3) postulated that flutter could be beneficially suppressed by use of active control systems. However, only about 10 years ago was serious consideration given to elastic mode stabilization using active control systems. Initially, feasibility studies evaluated the advantages gained by incorporating active controls on long flexible body aircraft and missiles. (See refs. 4 to 6.) Additional analytical studies evaluated the potential of active control systems regarding gust alleviation for the B-52 (ref. 7) and mode stabilization for the XB-70 (ref. 8). Subsequent flight tests of the B-52 aircraft resulted in reduced gust loads and extension of the fatigue life of the aircraft (ref. 9). Also, flight tests of the XB-70 aircraft demonstrated reductions in fuselage vertical accelerations (ref. 10). As a result of this new technological base, active flutter-suppression methods are now feasible. Supporting evidence is given in some recent analytical feasibility studies (refs. 11 to 16) and survey papers (refs. 17 to 23) by leading authorities. In many instances, analytical studies suggest that sizable weight savings are possible by using active flutter-suppression systems as opposed to the normal passive flutter control methods.

A method for flutter suppression using active controls proposed by E. Nissim (ref. 24) is based on aerodynamic energy considerations. This approach states that a necessary and sufficient condition for flutter prevention is that for all oscillatory motions of an elastic system in an airstream, positive work must be done by the system on the surrounding airstream. By appropriately equipping an elastic system with aerodynamic control surfaces whose deflections are related to motions of the system by a control law, it is theoretically possible to increase the flutter speed of the system. Since this energy approach to flutter suppression appeared to be promising, a wind-tunnel model program was initiated at the NASA Langley Research Center to evaluate this method experimentally. The specific purpose of this report is to present the significant results of this model study. Some earlier results of this study are reported in references 22 and 25 to 29.

The wind-tunnel model used for the active flutter-suppression program is a simplified version of a proposed supersonic transport wing design. The model was equipped with an active flutter-suppression system consisting of hydraulically operated leading-edge and trailing-edge control surfaces. Each control surface was actuated by feedback signals from two accelerometers which sensed the wing surface motion. This model was used to evaluate experimentally three control laws that were derived from aerodynamic energy considerations. The first two control laws used both the leading-edge and trailing-edge control surfaces. The third control law used only the trailing-edge control surface. Experimental flutter data were obtained in the Langley transonic dynamics tunnel at Mach numbers of 0.6, 0.7, 0.8, and 0.9. Results for both the flutter-suppression system oper-

ating (closed loop) and not operating (open loop) were obtained. These data were correlated with analytical flutter calculations based on doublet-lattice aerodynamics and experimentally determined mode shapes, generalized masses, and natural frequencies for the first nine wing modes. The analytical formulation of the flutter equations of motion is presented in appendix A. Analog implementation of the control law equations is given in appendix B. Descriptions of three different methods for determining the flutter speed by measuring and analyzing the model subcritical response (both open loop and closed loop) are presented in appendix C.

SYMBOLS

A_i, B_i, C_i, D_i constant coefficients (see eq. (A5))

$A_{ij}, A_{i\delta}, A_{i\beta}$ see equation (A7)

$[A_R], [A_I]$ real and imaginary unsteady aerodynamic-force matrix, respectively

a high pass filter break frequency, rad/s

B bulk modulus of hydraulic fluid

b reference semichord at $y = 0.933$ m (see fig. 1), 0.316 m

b_m one-half mean geometric chord of wing, 0.596 m

b_r reference semichord at $y = 0$, 0.882 m

C_A actuator torque constant

C_{ij}, G_{ij} control law coefficients (see eq. (A4))

$[C], [G]$ real and imaginary control law matrix (see fig. 1)

c wing streamwise chord

D_{EQ} equivalent viscous damping coefficient of actuator and hydraulic fluid

$\{F\}$	generalized force matrix
f	flutter frequency, Hz
f_2	frequency of second structural vibration mode, Hz
g	structural damping coefficient
h(x,y,t)	vertical displacement of wing, positive down
h_1,h_2	vertical displacement at 30 percent and 70 percent of the wing reference chord, respectively (see fig. 1)
I_{EQ}	equivalent rotary inertia of actuator vane and hydraulic fluid
I_S	rotary inertia of control surface with respect to its hinge line
I_V	servovalve current
[K]	generalized stiffness matrix
K_A	servovalve amplifier gain
K_P	hydraulic fluid load pressure feedback gain
K_S	torsional spring constant of control surface shaft
K_V	no-load flow gain of servovalve
K_δ	actuator shaft position feedback gain
k	reduced frequency, $b_r\omega/V$
M	Mach number
[M]	generalized mass matrix

M_i	generalized mass of ith vibration mode (i = 1, 2, . . .)
m	total mass of wing model, includes semispan wing and nacelles, 27.175 kg
m(x,y)	mass distribution
P_L	hydraulic fluid load pressure
$\Delta p(x,y,t)$	pressure distribution
Q	hydraulic fluid flow rate from the servovalve
$Q_i(t)$	generalized aerodynamic force
$\{q\}$	generalized displacement vector
q_R, q_I	real and imaginary generalized displacements
$q_i(t)$	generalized displacement of ith vibration mode
q_∞	dynamic pressure, Pa
S	reference area, m^2
s	Laplace variable
t	time, s
[U]	aerodynamic energy matrix in equation (2)
$[\overline{U}]$	complex conjugate of the matrix [U]
$[\overline{U}]^T$	transpose of $[\overline{U}]$
V	free-stream velocity, m/s
V_{CA}	command voltage to trailing-edge actuator loop

$(V_C)_{LE}$	command voltage to leading-edge control system
$(V_C)_{TE}$	command voltage to trailing-edge control system
V_δ	voltage proportional to control surface position
v	volume of a conical frustum having wing root chord as base diameter, wing tip chord as upper diameter, and wing semispan as height, 1.181 m^3
v_a	volume of hydraulic fluid on one side of actuator
x,y	streamwise and spanwise coordinates, respectively, origin at wing apex
$Z_i(x,y)$	normalized vertical deflection in ith vibration mode
α	angle of attack at section A-A ($y = y_1$) (see fig. 1)
$\beta,\hat{\beta}$	leading-edge control deflection in radians and degrees, respectively
$\delta,\hat{\delta}$	trailing-edge control deflection in radians and degrees, respectively
δ_V	apparent damping ratio of the open-loop servovalve
δ_{ij}	Kronecker delta (0 when $i \neq j$; 1 when $i = j$)
$\delta_{t,c}$	deflection command signal to trailing-edge control
η	nondimensional spanwise coordinate (see fig. 5)
λ	eigenvalues of matrix [U]
μ	mass-density ratio, $m/\rho v$
ξ	generalized coordinates associated with aerodynamic energy
ρ	density of test medium, kg/m^3

τ period of the sinusoidal input signal

Ω_r dependent variable, $\frac{\omega_r^2}{\omega^2}(1 + ig)$ (see eq. (A8))

ω circular frequency

ω_i circular frequency of ith structural vibration mode

ω_{NV} apparent undamped natural frequency of open-loop servovalve

ω_r arbitrary reference circular frequency, used second structural mode frequency of 103.04 rad/s

ω_S control surface natural rotation frequency

ω_2 circular frequency of second structural vibration mode

Subscripts:

f flutter

I imaginary value

R real value

Dots denote time derivatives and a circumflex denotes angular measurement given in degrees.

FLUTTER SUPPRESSION BASED ON AERODYNAMIC ENERGY CONSIDERATIONS

Flutter is a self-excited oscillation in which energy is absorbed by the lifting surface from the airstream. The state of stability of the system is indicated by the sign of the work per cycle done by the system on the airstream when the lifting surface undergoes

an oscillatory motion. The use of energy techniques to investigate the stability of an aeroelastic system is not new (see ref. 30); however, a recent contribution to the area of flutter suppression is the development of an aerodynamic energy criterion by Nissim (ref. 24). This criterion states that a necessary and sufficient condition for the prevention of flutter is that for all oscillatory motions of an elastic system in an airstream, positive work must be done by the system on the surrounding airstream. A brief summary of of the salient points brought out in reference 24 is presented in the following discussion.

Consider the equations of motion for a system with n degrees of freedom:

$$\{F\} = -\omega^2\left[[M] + \pi\rho b^4 S\left([A_R] + i[A_I]\right)\right]\{q\} + [K]\{q\} \tag{1}$$

where, at flutter, the generalized force $\{F\} = 0$ and ω is the circular frequency of oscillation; $[M]$ is the mass matrix; $[A_R]$ and $[A_I]$ are the real and imaginary unsteady aerodynamic-force matrices, respectively; $[K]$ is the structural stiffness matrix; ρ is the fluid density; S and b are a reference area and length, respectively; and $\{q\}$ is the generalized displacement vector.

Nissim shows that the work per cycle W done by the system on the airstream can be written as

$$W = \frac{1}{2}\pi^2\rho b^4 S\omega^2\left\{q_R - iq_I\right\}[U]\{q_R + iq_I\} \tag{2}$$

where

$$[U] = \left[-\left([A_I] + [A_I]^T\right) + i\left([A_R] - [A_R]^T\right)\right]$$

A positive value for W indicates a transfer of energy from the system to the airstream and hence stability. The matrix $[U]$ is Hermitian (that is, $[\overline{U}]^T = [U]$) and therefore possesses real eigenvalues. By use of these eigenvalues, it is shown in reference 24 that the energy input per cycle into the airstream can be reduced to a principal quadratic form as

$$W = \frac{1}{2}\pi^2\rho b^4\omega^2 S\left[\lambda_1\left(\xi_{R_1}^2 + \xi_{I_1}^2\right) + \lambda_2\left(\xi_{R_2}^2 + \xi_{I_2}^2\right) + \ldots + \lambda_n\left(\xi_{R_n}^2 + \xi_{I_n}^2\right)\right] \tag{3}$$

where $\lambda_1, \lambda_2, \ldots, \lambda_n$ are the eigenvalues of the matrix $[U]$ and ξ denotes generalized

coordinates associated with the aerodynamic energy. It can be seen from equation (3) that the work W will always be positive if all the eigenvalues λ are positive. Therefore, a sufficient but not necessary condition for flutter stability is that all the λ terms are positive. A notable characteristic of the energy method is that the criterion for flutter stability is determined by the characteristics of the aerodynamic-force matrices alone. Therefore, if a particular system has undesirable flutter characteristics (that is, too low a flutter speed), the flutter characteristics can be improved if a mechanism can be found which changes the [U] matrix in an appropriate manner. One such mechanism is the addition of active control surfaces to the basic system. The motions of these surfaces generate aerodynamic forces which modify the aerodynamic terms in the [U] matrix for the basic system. For flutter suppression the control surface deflections are related by a control law to the plunging and pitching motion of the main surface. Nissim points out in reference 24 that a suitable configuration is one employing both leading-edge and trailing-edge controls since the two working together provide independent control of lift and pitching moment.

A basic control law was derived by Nissim in reference 24 for such a suitable configuration and is shown in figure 1. This basic control law relates the control surface deflections β and δ to the wing motions h and α through a set of coefficients. The implementation of this control law in a three-dimensional flutter analysis is developed in appendix A.

$$\begin{Bmatrix} \beta \\ \delta \end{Bmatrix} = \begin{bmatrix} C_{11} & C_{12} \\ C_{21} & C_{22} \end{bmatrix} \begin{Bmatrix} \frac{h_1}{b} \\ \alpha \end{Bmatrix} + i \begin{bmatrix} G_{11} & G_{12} \\ G_{21} & G_{22} \end{bmatrix} \begin{Bmatrix} \frac{h_1}{b} \\ \alpha \end{Bmatrix}$$

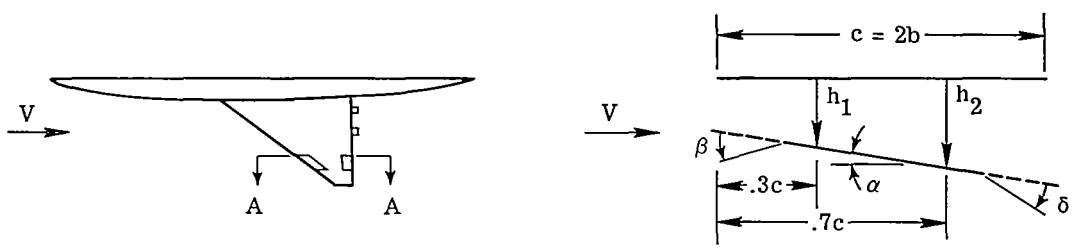

Section A-A

Figure 1.- Basic control law parameters.

DELTA-WING MODEL PROGRAM

Background

An early evaluation of the practical aspects of the aerodynamic energy concept was made in an analytical study of the application of this concept to a supersonic transport configuration. (See ref. 25.) The wing configuration used in this study is shown in figure 2(a). Three spanwise locations of aerodynamic control surfaces were considered in the investigation, designated I, II, and III in the figure. Each configuration consisted of both leading-edge and trailing-edge control surfaces activated by sensors located on the wing at the 30-percent and 70-percent midspan chord of each spanwise location. The results showed improvement in flutter speed of 21 percent for configuration I, 28 percent for configuration II, and 11 percent for configuration III. Additional calculations showed that the combined use of configurations I and II working concurrently produced an improvement in flutter speed in excess of 41 percent. These results are illustrated in the root locus plot shown in figure 2(b).

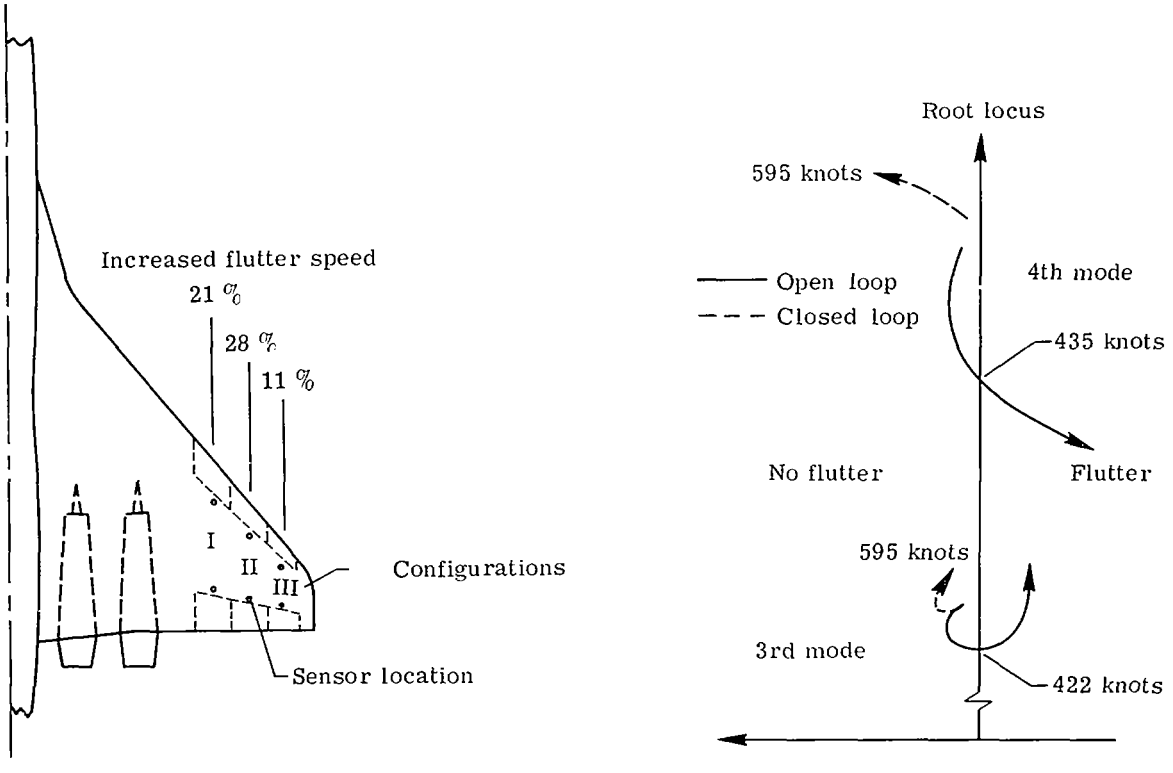

(a) Results for three different spanwise configurations.

(b) Results for configurations I and II working concurrently.

Figure 2.- Calculated effectiveness of aerodynamic energy concept flutter-suppression systems.

Since these analytical studies indicated that active control surfaces were very effective in increasing flutter speeds, a combined experimental-analytical research program was undertaken to verify this concept. This program used a semispan delta-wing model which was a simplified version of an early supersonic transport configuration. The model incorporated both leading-edge and trailing-edge control surfaces.

Model Development

Design considerations.- It was considered desirable to have the present model representative of current or proposed high-speed configurations. Consequently, the model design was based on a low-aspect-ratio, clipped-delta-wing configuration similar to a proposed supersonic transport. The design objective was to have a relatively simple and inexpensive model which would be of adequate size to incorporate control surfaces with an oscillatory drive mechanism, would simulate the flutter characteristics of the full-scale prototype design, and would flutter within the middle operating range of the wind tunnel. Pilot model studies without active controls which provided needed design information for the active control model are described in reference 31.

A photograph of the present semispan delta-wing model mounted in the Langley transonic dynamics tunnel is presented in figure 3. The model geometry is shown in figure 4. The aspect-ratio-1.28 model had a leading-edge sweepback angle of 50.5°, a taper ratio

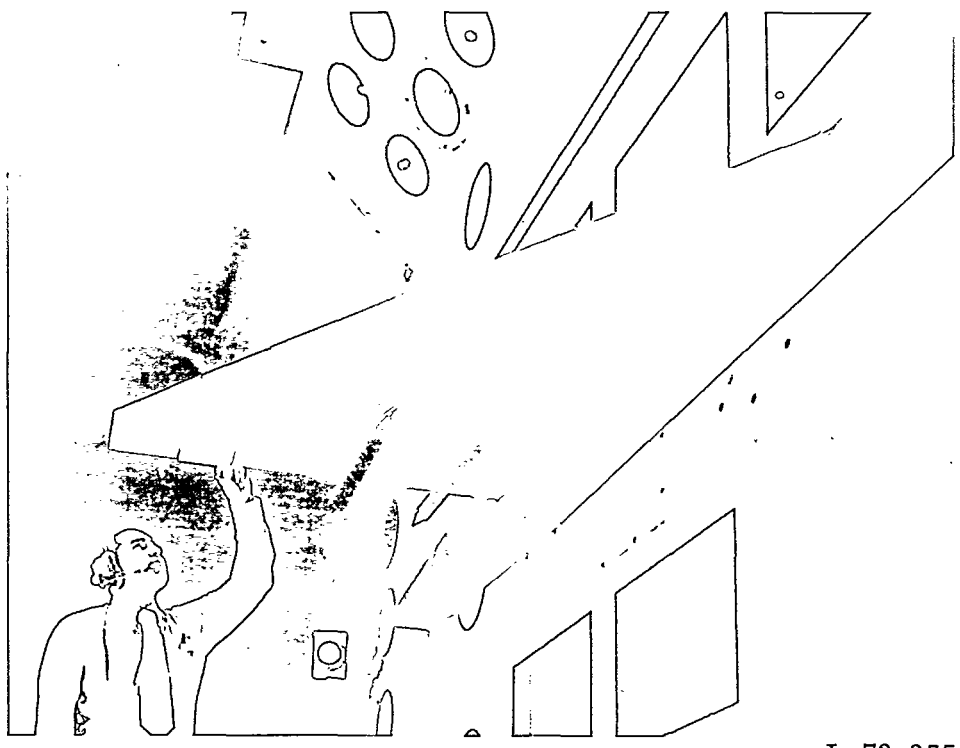

L-73-355

Figure 3.- Delta-wing flutter-suppression model.

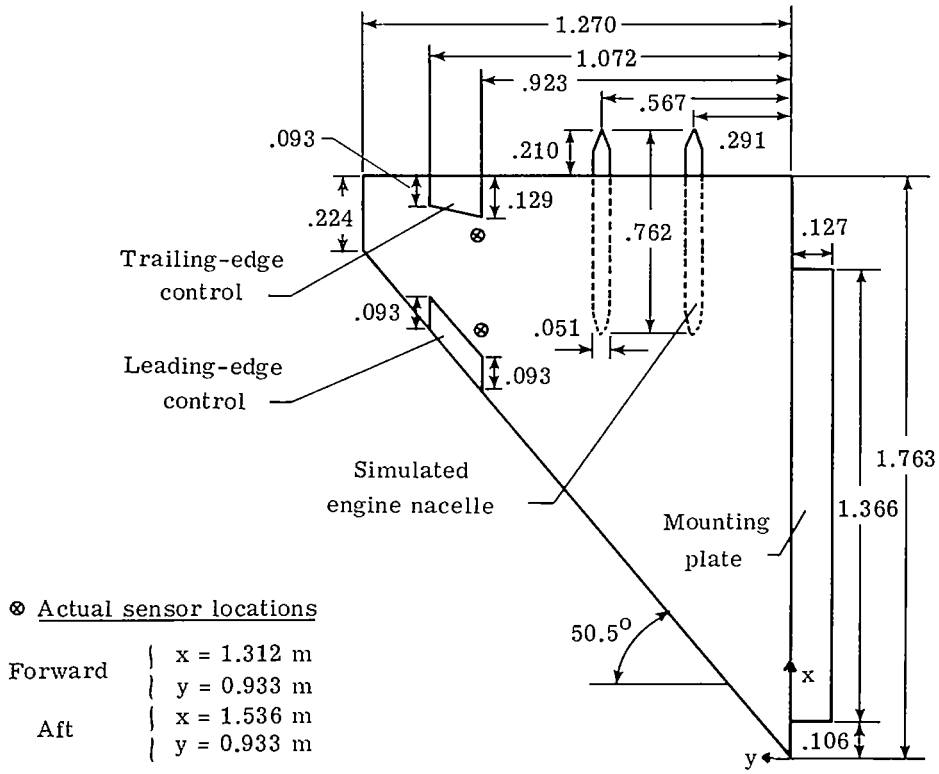

Figure 4.- Sketch of delta-wing model. All linear dimensions are in meters.

of 0.127, and a circular-arc airfoil section with a ratio of thickness to chord of 0.03. Two high-fineness-ratio bodies were mounted on the wing lower surface to simulate engine nacelles. A rigid sidewall mounting block was used to simulate a fuselage fairing. This mounting arrangement placed the wing root outside the tunnel-wall boundary layer. The model was equipped with both leading-edge and trailing-edge control surface. Each control surface was controllable by an electrohydraulic servo actuation system.

Construction.- The construction of the delta-wing model was relatively simple and inexpensive. It consisted of a primary load-carrying plate structure covered with balsa wood that was contoured to the desired airfoil shape.

Wing: A solid aluminum-alloy rectangular plate was tapered in thickness in the spanwise direction by a chemical milling process. This tapered plate was then covered with a rubber compound and with the aid of a template, holes were cut into the rubber compound to expose portions of the metal plate. Chemical milling was again used to cut holes through the exposed metal to simulate a spar and rib structure. From this fabricated plate structure, the proper planform shape was sawed out to obtain the desired internal wing structure, or insert, as illustrated in figure 5. The insert was covered with balsa wood and properly contoured to the desired airfoil section. Finally, a single layer of 0.025-mm fiber-glass cloth was doped to the wood for protection and handling purposes.

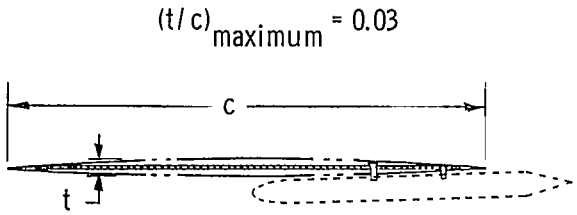

Section A-A

Internal plate thickness, m		
$\eta = 0.0$	$\eta = 0.53$	$\eta = 1.0$
0.016408	0.006502	0.000711

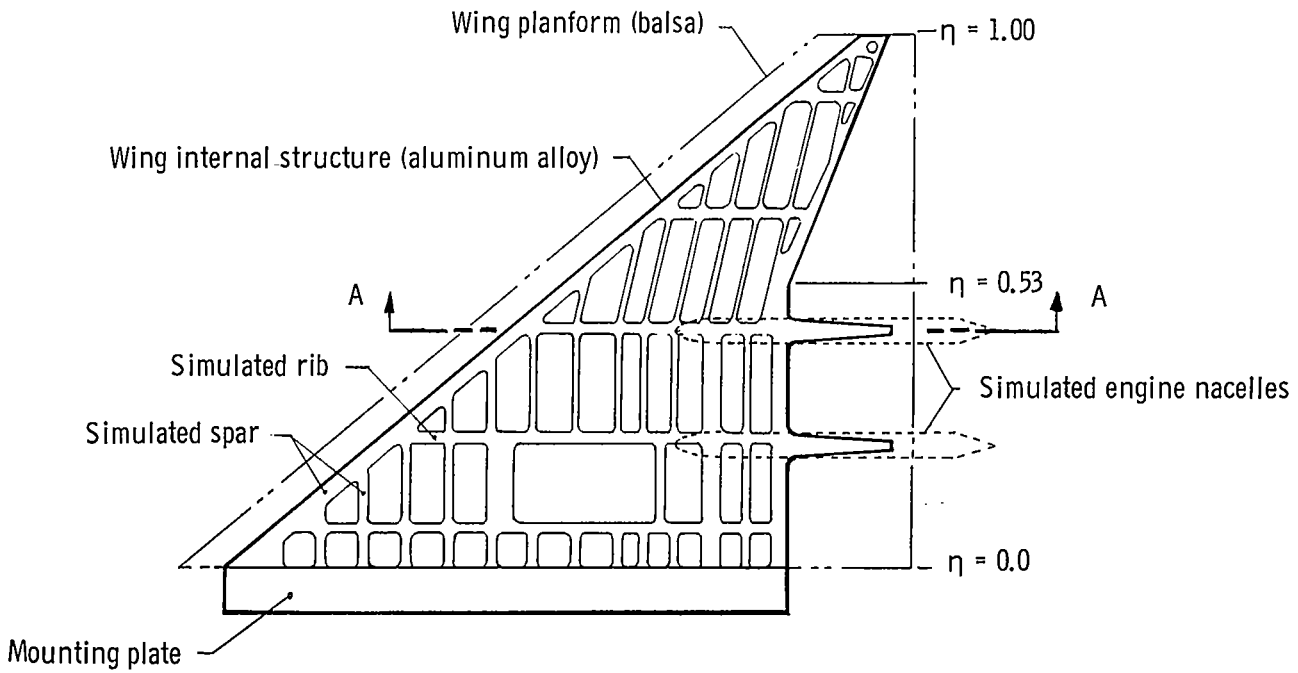

Figure 5.- Typical details of model construction.

Two identical slender streamline bodies were constructed to simulate engine nacelles. Each nacelle consisted of a cylindrical centerbody with an ogive nose and a conical tail fairing. The centerbody was made of a thick-wall steel tube ballasted with lead weights, whereas the nose and tail fairings were made of balsa wood.

Control surfaces: Both the leading-edge and trailing-edge control surfaces were constructed of balsa wood with two 1.6-mm hardwood stiffeners (chordwise) located at the one-third and two-thirds control surface span. A combination of aluminum and stainless steel 3.2-mm tubing was glued into the balsa wood to form an axle at the rotation axis of each control surface. Each surface axle was suspended by a precision ball bearing on the outboard end and by the actuator shaft on the inboard end. The trailing-edge control surface chord was approximately 20 percent of the local wing chord, whereas the leading-edge control surface chord varied from about 15 percent of the wing local chord inboard to 20 percent of the wing chord outboard. Both controls were located approximately between 73 percent and 84 percent of the wing span. These surface locations are approximately the same as configuration II of figure 2.

Actuator: Initially, an attempt was made to mechanize the control surfaces with an electro-mechanical system. The original mechanization consisted of a quick-response high-torque electric dc motor, mounted externally to the model, which was connected to and drove the control surface through a drive shaft. A problem was encountered with the wind-up of the long drive shaft. After extensive research it was then decided to develop an electrohydraulic servo system so that the actuator could be located next to the control surface; thus the shaft wind-up problem was eliminated.

Prior to abandoning the electro-mechanical control system which was already installed in the delta-wing model, a wind-tunnel study was conducted (ref. 20) to measure static hinge moments on the leading-edge and trailing-edge control surfaces at transonic Mach numbers. Previous hinge moments calculated by a variety of methods produced a wide range of values. Therefore, measured hinge moments were very valuable to the final actuator design and to the analytical studies as discussed later in appendix A. To match the desired torque, small size, and lightweight requirements of the present model, it was necessary to design and fabricate special actuators. Two special miniature hydraulic actuators were successfully designed and fabricated as described in reference 32. A photograph of an actuator installed in the delta-wing model is shown in figure 6(a). Briefly, the actuator consisted of a closed compartment separated into two chambers by a self-sealing vane attached to a shaft and supported by two miniature precision ball bearings. A photograph of the actuator components is presented in figure 6(b). Shaft rotation is obtained by applying a differential hydraulic pressure between the two chambers. The actuator has a mass less than 60 grams and is capable of providing 4.52 N-m torque output over the frequency range from 0 to 25 Hz with a 6.9 MPa supply pressure. The actu-

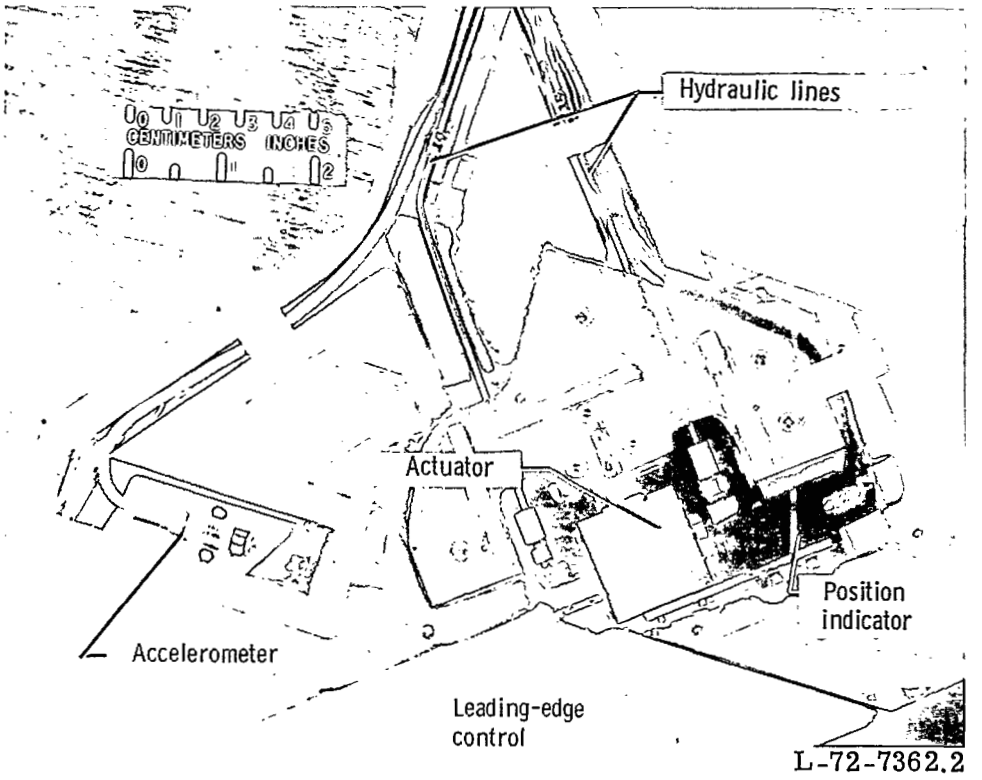

(a) Actuator installed in model.

Figure 6.- Delta-wing hydraulic actuation system.

ator angular displacement capability was approximately $\pm 9.0^{\circ}$. The development of these miniature actuators represents a significant contribution to active control modeling technology and was a major contribution to the success of the current active flutter-suppression study.

Control surface position indicators: Normally, small precision potentiometers are used for accurate angular measurements of control surfaces. The smallest known potentiometer (1.27-cm diameter) was not usable with the present model because of size and space constraints. Therefore, it was necessary to design and fabricate special control surface angular position indicators. The new position indicator is a rather simple device that uses two silicon solar cells (separated by 0.25-mm gap) mounted on a common base. The device is attached to one end of the actuator shaft. A stationary light source illuminates one half of each solar cell by use of a properly located baffle. As the actuator shaft rotates from a zero null position, one solar cell receives more illumination than the other and thereby a differential voltage between the two cells is produced which is proportional to the shaft rotational angle. This solar cell position indicator proved to be not only linear but also was very accurate in that total system calibrations of solar cells were repeatable to within 0.10°. Reliability and durability of the device are evident by the fact that no failures occurred and no significant change in performance characteristics occurred

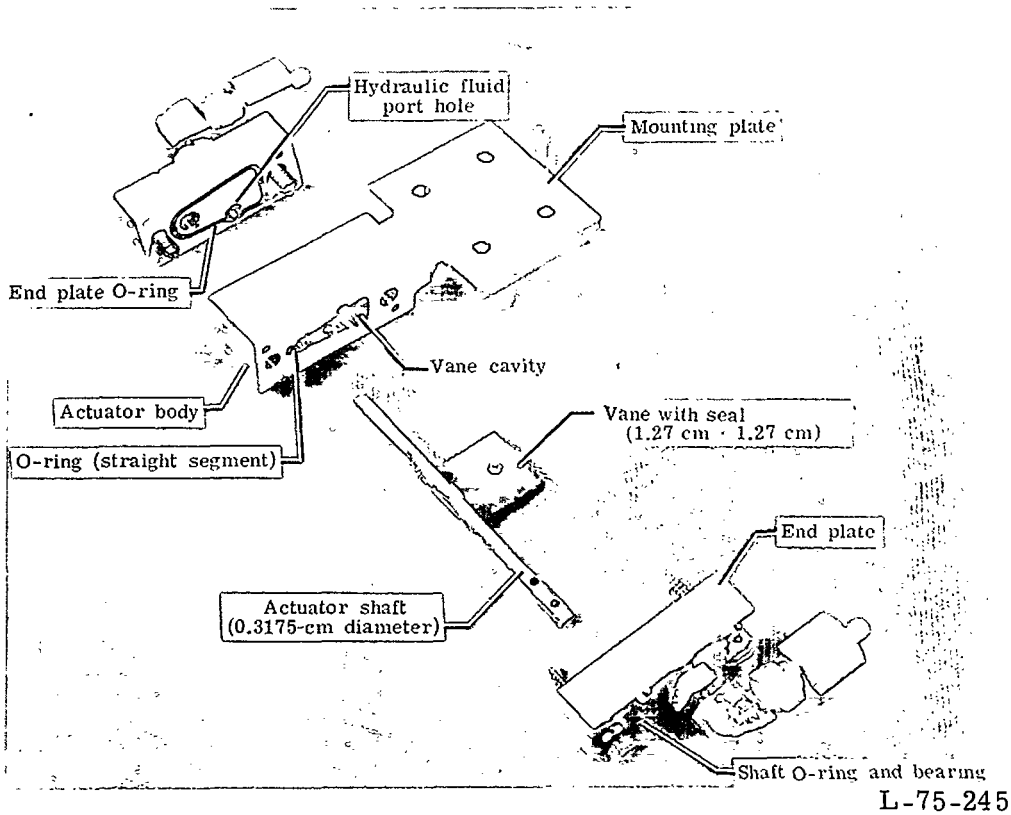

(b) Miniature hydraulic actuator components.

Figure 6.- Concluded.

during more than 2 years of operation which included extensive laboratory tests and several wind-tunnel flutter tests. The successful development of the solar cell position indicator is another contribution to active control modeling technology.

Model physical properties.- The delta-wing model was not amenable to structural analysis because of the uncertainties of modeling the stiffness properties of the glued-on balsa wood airfoil. Hence, for the purpose of formulating an adequate math model to be used in the subsequent flutter analysis, the first nine structural mode shapes, generalized masses, and natural frequencies were measured.

The mode shapes were obtained by using a noncontact deflection-measuring device described in reference 33. Deflection values were measured at 54 stations on the wing surface (six spanwise stations and nine chordwise stations). Six additional points were added to define the engine nacelle motion of the more complex higher modes. Station numbers, coordinate locations, and nondimensional vertical displacements for the natural modes are presented in table I. Generalized masses were determined by using the method of displaced frequencies described originally in reference 34 and, more recently, in reference 35. The generalized masses and frequencies are presented in table II. Some addi-

tional total mass and inertia properties are presented in table III. Computer graphic display of the mode shapes is presented in figure 7.

TABLE I.- MEASURED MODE SHAPE DATA FOR DELTA-WING MODEL

[x and y are in meters. Z_1 to Z_9 are normalized to station 50]

Sta.	x	y	Z_1	Z_2	Z_3	Z_4	Z_5	Z_6	Z_7	Z_8	Z_9
1	.264	.153	.009	.007	-.001	-.003	.010	-.016	.022	.034	.041
2	.438	.153	.008	.009	-.009	-.007	.009	-.025	.031	.049	.063
3	.611	.153	.012	.010	-.015	-.011	.018	-.023	.036	.057	.071
4	.785	.153	.016	.009	-.024	-.015	.033	-.014	.040	.061	.066
5	.974	.153	.021	.005	-.027	-.013	.063	.010	.033	.048	.036
6	1.164	.153	.027	-.001	-.034	-.011	.103	.038	.030	.034	-.003
7	1.337	.153	.035	-.009	-.046	-.004	.143	.058	.028	.025	-.047
8	1.511	.153	.036	-.026	-.070	.027	.154	.050	.024	.018	-.082
9	1.684	.153	.051	-.053	-.116	.082	.124	.014	.021	.009	-.083
10	.607	.450	.038	.044	-.151	-.095	-.022	-.228	.193	.323	.384
11	.740	.450	.053	.046	-.176	-.106	-.011	-.207	.194	.319	.351
12	.874	.450	.070	.041	-.187	-.112	.014	-.150	.173	.280	.284
13	1.008	.450	.090	.033	-.189	-.110	.043	-.063	.141	.216	.199
14	1.154	.450	.112	.017	-.159	-.099	.083	.048	.100	.134	.097
15	1.300	.450	.137	-.004	-.108	-.085	.119	.161	.060	.050	-.002
16	1.434	.450	.164	-.041	-.144	-.053	.135	.234	.039	.008	-.087
17	1.568	.450	.186	-.094	-.091	-.006	.105	.208	.039	.006	-.138
18	1.702	.450	.234	-.160	-.012	.049	.055	.118	.056	.040	-.193
19	.918	.721	.174	.130	-.425	-.246	-.229	-.608	.265	.466	.290
20	1.016	.721	.209	.125	-.406	-.237	-.221	-.530	.194	.362	.186
21	1.114	.721	.235	.114	-.352	-.210	-.189	-.389	.115	.243	.107
22	1.212	.721	.264	.103	-.301	-.187	-.159	-.257	.041	.124	.050
23	1.319	.721	.296	.085	-.225	-.157	-.114	-.101	-.039	-.011	.037
24	1.425	.721	.337	.060	-.135	-.125	-.072	.040	-.110	-.135	.070
25	1.523	.721	.378	.032	-.039	-.095	-.044	.142	-.169	-.233	.126
26	1.621	.721	.412	0.000	.066	-.066	-.016	.229	-.228	-.326	.194
27	1.719	.721	.449	-.036	.180	-.036	.010	.304	-.284	-.409	.272
28	1.182	.950	.428	.305	-.305	-.197	-.572	-1.107	-.024	.263	-.001
29	1.250	.950	.436	.304	-.277	-.150	-.500	-.971	-.072	.157	-.575
30	1.317	.950	.476	.307	-.191	-.100	-.434	-.805	-.123	.050	-.551
31	1.384	.950	.514	.312	-.095	-.043	-.339	-.603	-.166	-.056	-.466
32	1.457	.950	.547	.319	.018	.025	-.231	-.372	-.212	-.174	-.355
33	1.531	.950	.580	.326	.131	.091	-.120	-.127	-.255	-.294	-.232
34	1.598	.950	.605	.329	.229	.152	-.026	.090	-.295	-.400	-.117
35	1.665	.950	.642	.345	.346	.228	.099	.337	-.304	-.482	.048
36	1.733	.950	.688	.352	.463	.294	.209	.594	-.352	-.612	.185
37	1.383	1.124	.667	.606	.102	.263	-.320	-.945	.021	.237	-.950
38	1.427	1.124	.717	.619	.207	.269	-.178	-.694	.057	.224	-.751
39	1.471	1.124	.734	.642	.307	.342	-.048	-.438	.096	.211	-.559
40	1.515	1.124	.758	.670	.409	.432	.092	-.189	.130	.195	-.354
41	1.563	1.124	.791	.686	.518	.509	.242	.092	.168	.187	-.116
42	1.611	1.124	.815	.707	.619	.585	.384	.363	.209	.158	.112
43	1.655	1.124	.839	.722	.710	.647	.519	.620	.233	.125	.325
44	1.699	1.124	.863	.724	.798	.712	.646	.866	.265	.097	.538
45	1.743	1.124	.893	.748	.886	.774	.792	1.127	.303	.072	.761
46	1.508	1.233	.921	.915	.674	.748	.487	.066	.696	.868	.037
47	1.537	1.233	.920	.957	.747	.803	.598	.291	.767	.897	.246
48	1.567	1.233	.946	.951	.829	.879	.734	.520	.839	.927	.505
49	1.596	1.233	.972	.974	.907	.925	.859	.737	.905	.961	.754
50	1.629	1.233	1.000	1.000	1.000	1.000	1.000	1.000	1.000	1.000	1.000
51	1.661	1.233	.994	1.009	1.074	1.067	1.144	1.268	1.051	1.033	1.272
52	1.690	1.233	1.017	1.034	1.178	1.122	1.290	1.511	1.143	1.066	1.505
53	1.720	1.233	1.019	1.035	1.235	1.155	1.410	1.720	1.196	1.075	1.766
54	1.750	1.233	1.051	1.040	1.294	1.220	1.531	1.950	1.251	1.096	1.975
55	1.709	.567	*	*	.242	-.041	-.006	-.073	.036	.056	.018
56	1.591	.567	*	*	.035	-.068	.043	.147	-.009	-.040	.030
57	1.473	.567	*	*	.113	-.095	.065	.240	-.023	-.069	.035
58	1.692	.291	*	*	.261	.211	-.077	-.032	.003	.017	.015
59	1.537	.291	*	*	.151	.056	.115	.120	.034	.026	-.118
60	1.382	.291	*	*	.105	-.018	.162	.144	.044	.037	-.092

*Deflections at stations 55 to 60 were not measured for modes 1 and 2.

TABLE II.- MEASURED FREQUENCY AND GENERALIZED MASS DATA FOR DELTA-WING MODEL

Mode	Natural frequency, Hz	Generalized mass, kg
1	7.8	1.536
2	16.4	.489
3	24.1	1.065
4	25.4	.720
5	38.2	1.885
6	43.3	.820
7	45.9	.351
8	48.2	2.520
9	58.1	1.445

TABLE III.- MEASURED MASS PROPERTIES

Wing:

Mass (outboard of $\eta = 0.0$, see fig. 5), kg 14.215

Inboard nacelle:

Mass, kg 6.480

Center of gravity, m . . . . . y = 0.291, x = 1.617

Pitch inertia about center of gravity, kg-m^2 . . . . . 0.147

Yaw inertia about center of gravity, kg-m^2 . . . . . 0.147

Outboard nacelle:

Mass, kg 6.480

Center of gravity, m . . . . . y = 0.568, x = 1.617

Pitch inertia about center of gravity, kg-m^2 . . . . . 0.147

Yaw inertia about center of gravity, kg-m^2 . . . . . 0.147

Wing plus both nacelles:

Mass, kg 27.175

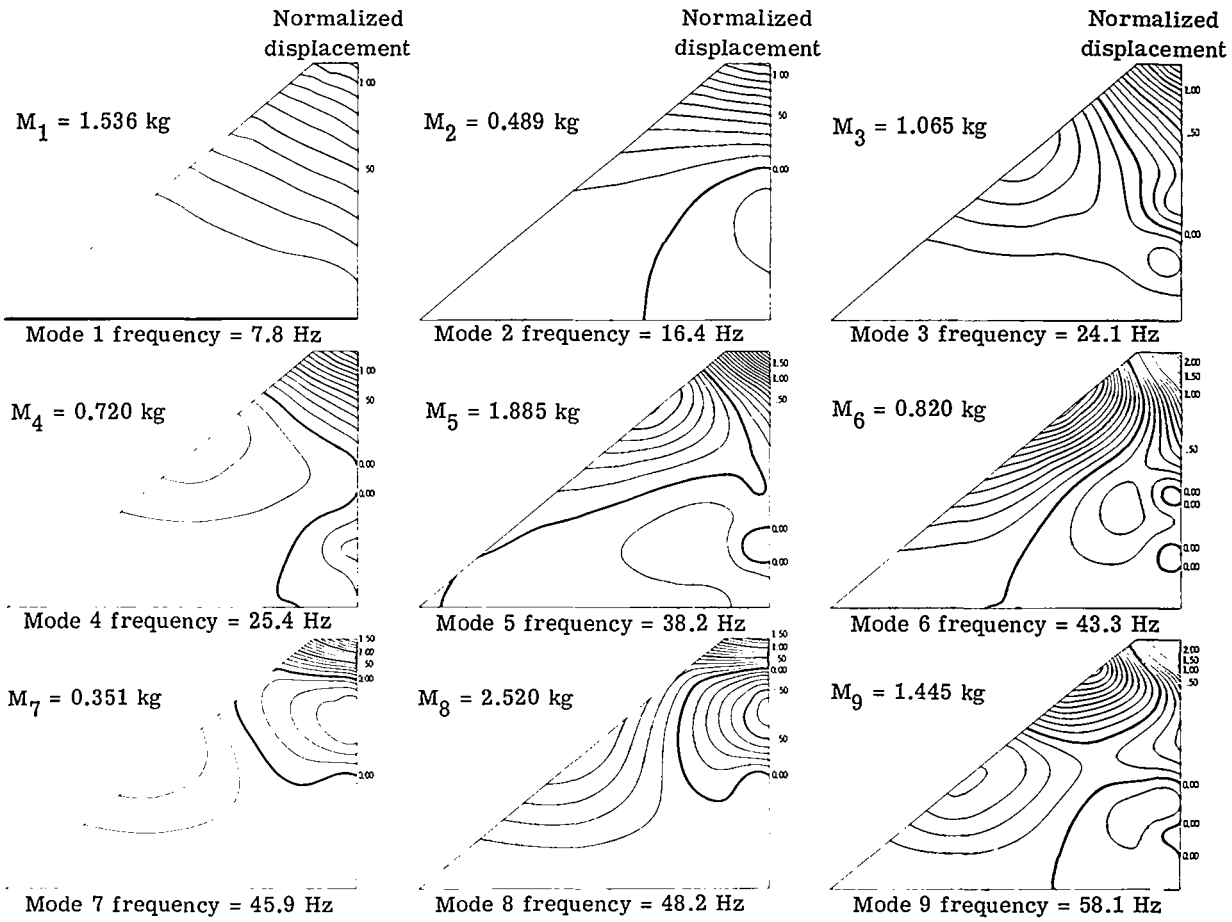

Figure 7.- Measured modal contours, generalized masses, and frequencies of natural vibration modes. Contour interval, 0.1 normalized displacement.

CONTROL LAWS

Three variations of the basic control law (fig. 1) were implemented and tested on the model. The first control law used (control law A) was similar to that given in reference 24 and used both leading-edge and trailing-edge control surfaces. Feedback gains were determined by using two-dimensional unsteady aerodynamic theory. Control law A was used as a first step in experimentally validating the aerodynamic energy concept.

In addition, two sets of feedback gains (referred to as control laws B and C) were developed by using three-dimensional unsteady aerodynamic theory. The design criterion for control laws B and C was to raise the flutter boundary at $M = 0.90$ a minimum of 30 percent in dynamic pressure. Control law B used both leading-edge and trailing-edge control surfaces whereas control law C used only a trailing-edge control surface. The main reason prompting the choice of control law C is the potential difficulty associated with any leading-edge control surface. The three control laws are given in table IV.

TABLE IV.- DELTA-WING MODEL CONTROL LAWS

WITH ORIGINAL ANALYTICAL VALUES

Control law A

$$\begin{Bmatrix} \beta \\ \delta \end{Bmatrix} = \begin{bmatrix} 0 & 5.6 \\ 0 & -1.4 \end{bmatrix} \begin{Bmatrix} h_1/b \\ \alpha \end{Bmatrix} + i \begin{bmatrix} 0 & 1.5 \\ 0.6 & 0.2 \end{bmatrix} \begin{Bmatrix} h_1/b \\ \alpha \end{Bmatrix}$$

Control law B

$$\begin{Bmatrix} \beta \\ \delta \end{Bmatrix} = \begin{bmatrix} 0 & 0 \\ 2.7 & -5.3 \end{bmatrix} \begin{Bmatrix} h_1/b \\ \alpha \end{Bmatrix} + i \begin{bmatrix} 0 & 6.0 \\ 4.0 & 2.0 \end{bmatrix} \begin{Bmatrix} h_1/b \\ \alpha \end{Bmatrix}$$

Control law C

$$\begin{Bmatrix} \beta \\ \delta \end{Bmatrix} = \begin{bmatrix} 0 & 0 \\ 2.7 & -5.3 \end{bmatrix} \begin{Bmatrix} h_1/b \\ \alpha \end{Bmatrix} + i \begin{bmatrix} 0 & 0 \\ 4.0 & 2.0 \end{bmatrix} \begin{Bmatrix} h_1/b \\ \alpha \end{Bmatrix}$$

Control Surface and Sensor Locations

By using control law A and three-dimensional unsteady aerodynamic theory, an analytical study (ref. 26) of the delta-wing model was performed to determine the best locations for both the control surfaces and motion sensors. The results of this study are presented in figure 8. The largest increase in flutter dynamic pressure occurs when the outboard control surfaces are used in conjunction with the outboard accelerometers. However, the practical implementation of the hardware on the model precluded this location. Therefore, the midspan control surfaces along with the inboard accelerometers for this strip were selected as the configuration to mechanize on the model. As shown in figure 8, a 26-percent increase in the flutter dynamic pressure is predicted when control law A is used. It should be noted that this analysis did not take into account the control surface aerodynamic correction as described in appendix A.

Synthesis

The analytical technique used to establish the gains for control laws B and C was generally along the lines discussed in reference 24. That is, the nine structural mode shapes were used as input to the doublet-lattice aerodynamic program to compute the terms of the Hermitian energy matrix [U]. (See eq. (2).) The control law gains were

Percent increase in flutter dynamic pressure

Surface location	Accelerometer location		
	Inboard edge	Center line	Outboard edge
Inboard strip	18	22	21
Midspan strip	26	17	8
Outboard strip	6	25	36

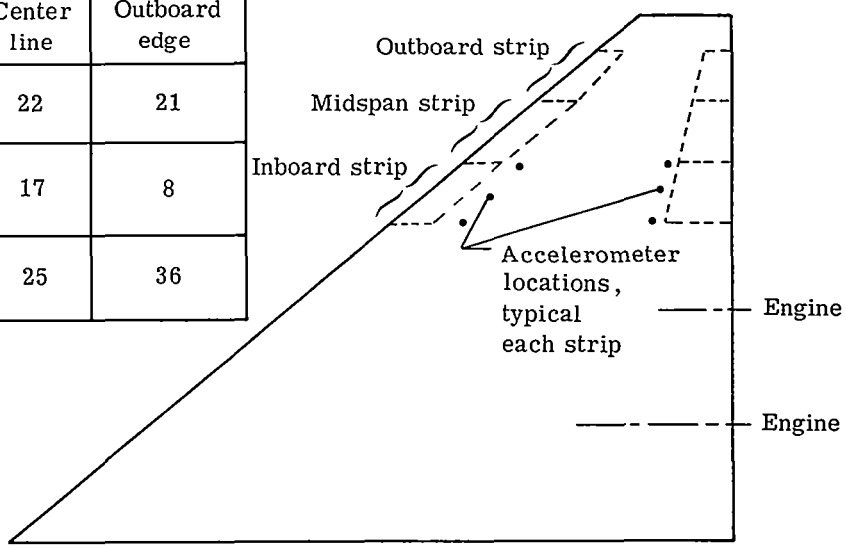

Figure 8.- Predicted effects of control surface and accelerometer locations on flutter dynamic pressure.

then varied and their effect on the eigenvalues of the [U] matrix computed. No effort was made to establish control surface displacements and rates.

Since the design criterion for control laws B and C was to increase the flutter dynamic pressure 30 percent, it was not necessary to insure that all the eigenvalues λ be made positive. Therefore, the eigenvalues were used as a guide by first determining which combination of gains had the largest effect on reducing the magnitude of the maximum negative eigenvalue. Then, once these gains were determined, the closed-loop flutter equations (appendix A) were solved and the new flutter velocity checked against the desired minimum flutter velocity. It was noted during these calculations that the set of gains which resulted in large reductions in the magnitude of the maximum negative eigenvalue also made significant reductions in the maximum positive eigenvalue. Therefore, those combinations of gains which gave the smallest magnitude of the negative eigenvalue could not be assumed to give the largest closed-loop flutter velocity. The effect of control laws A, B, and C on the eigenvalues λ as compared with the open-loop eigenvalues (for the first three flexible modes) is given in figure 9. The increase in flutter dynamic pressure for control laws A, B, and C are 12.5 percent, 630 percent, and 46.7 percent, respectively.

Implementation

Some of the physical components comprising the flutter-suppression system are shown in the photograph presented in figure 10. A simplified block diagram of the

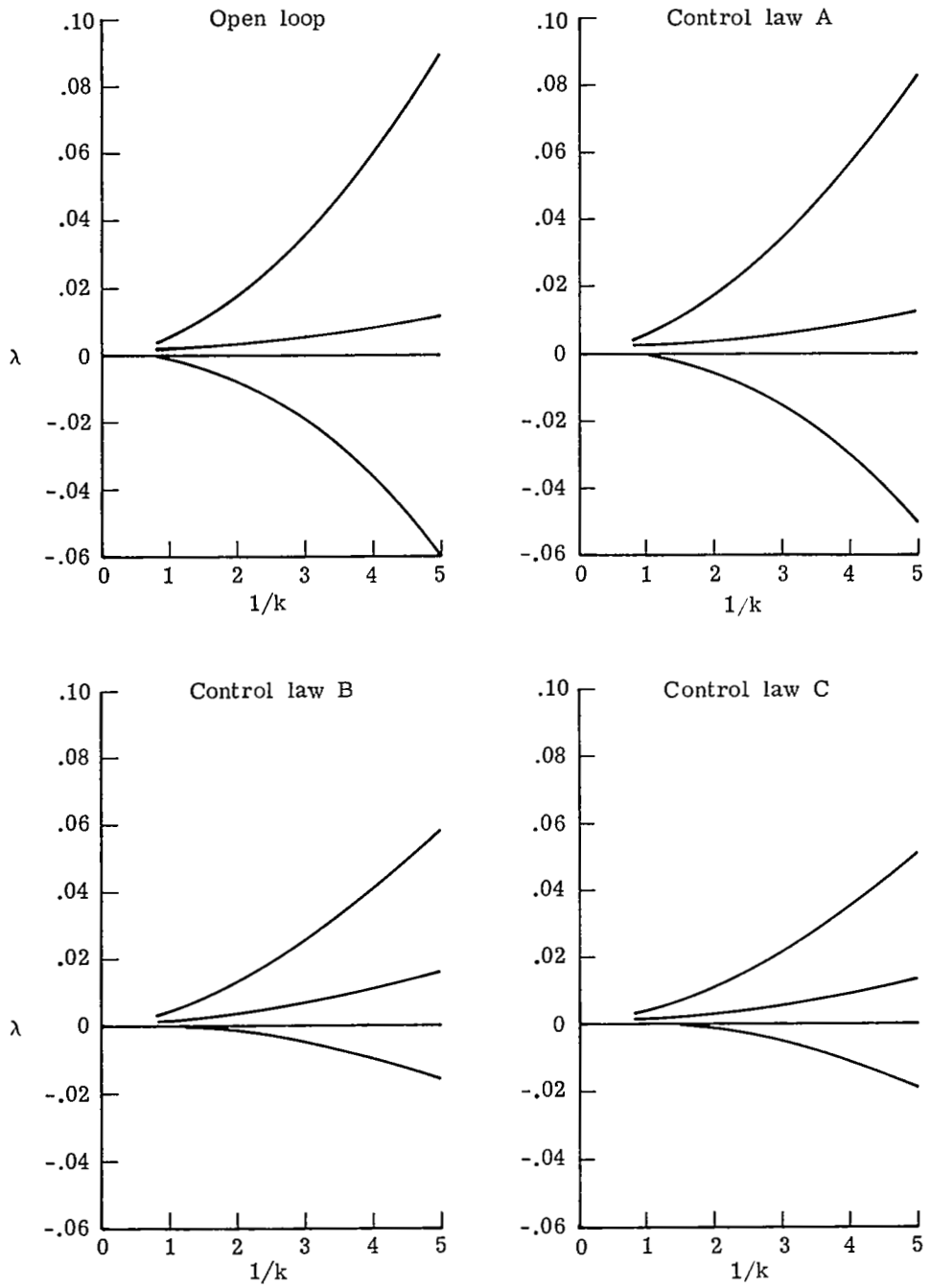

Figure 9.- Variation of λ with $1/k$.

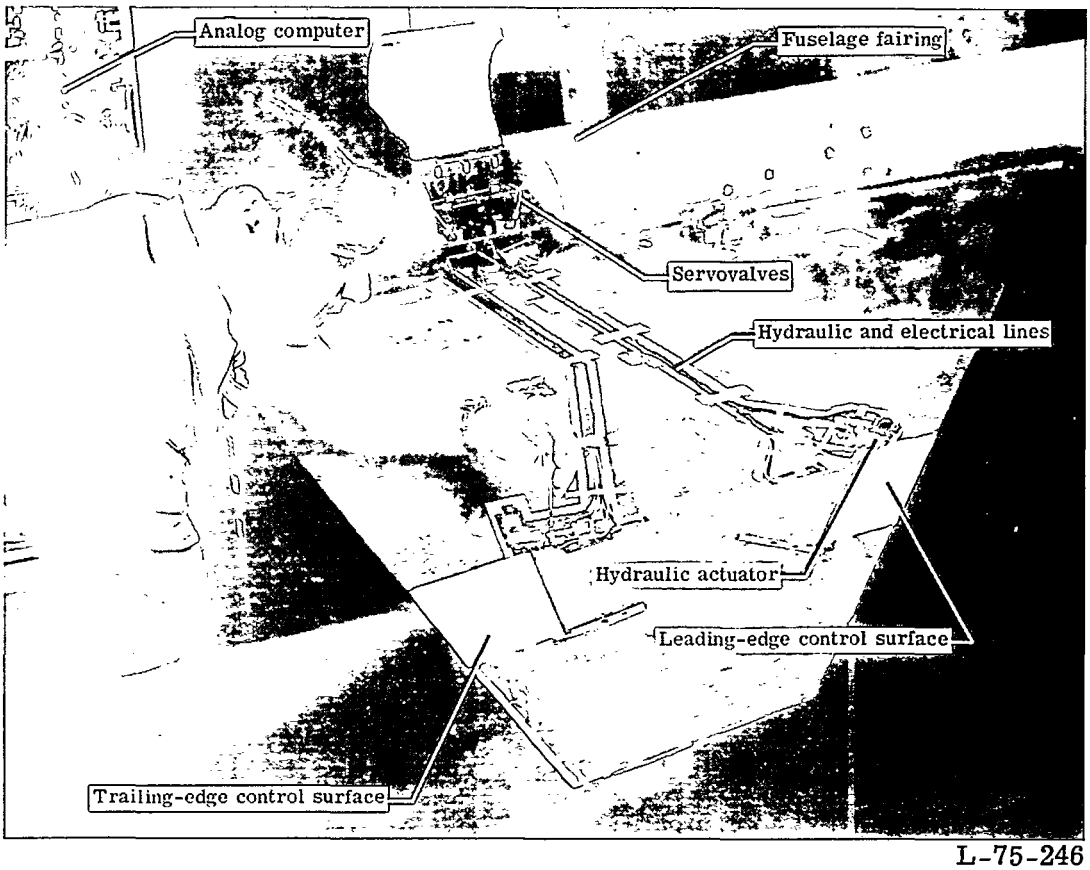

Figure 10.- Components of delta-wing flutter-suppression system.

mechanized flutter-suppression system is presented in figure 11. A more complete discussion of the flutter-suppression system mechanization is presented in appendix B. The wing motion was sensed at two points (see fig. 1) to determine rates and displacements by integrating the output of two accelerometers located in line with the inboard edges of the control surfaces at approximately 30 and 70 percent of the local chord. The basic form of the control law was programed on an analog computer which was located remotely from the model in the wind tunnel. Either control law A, B, or C was implemented by simply changing potentiometer settings on the analog computer corresponding to the gains for each control law. The accelerometer output signals were routed through signal conditioning equipment to the analog computer which processed the signals to determine the appropriate actuator command signals. These command signals were passed to hydraulic servovalves (mounted in the fuselage fairing at the model root, see fig. 10) which controlled the supply of hydraulic fluid to the control actuators. All electrical and hydraulic lines were routed to the actuators and sensors through trenches cut into the balsa wood which provided the aerodynamic contour for the model. Although not indicated in figure 11, provision for introducing external command signals to the trailing-edge control was provided in order to perform both open-loop and closed-loop frequency sweeps. For

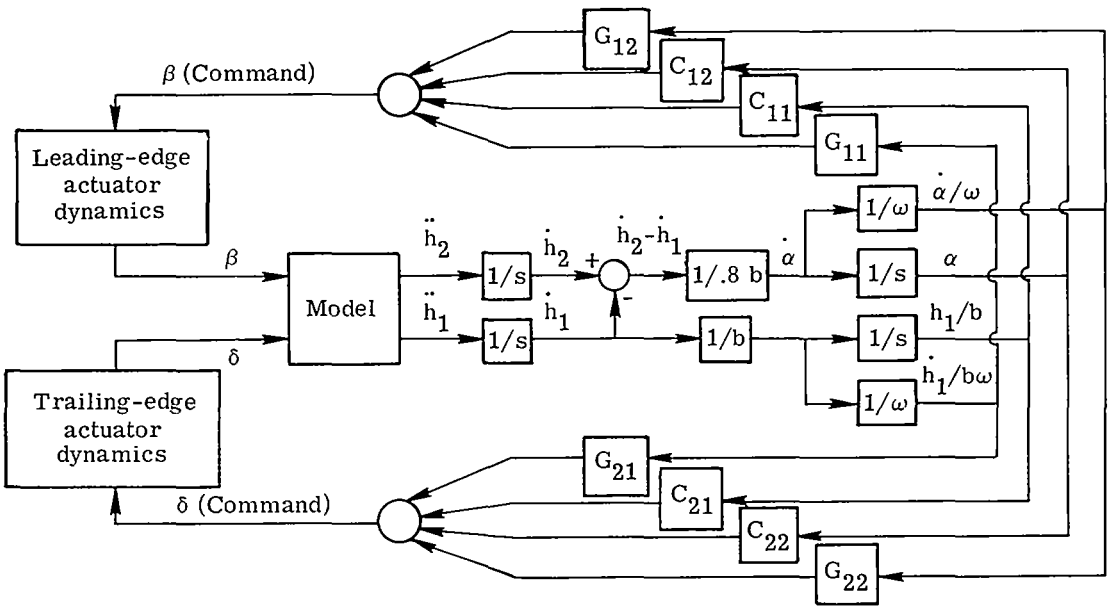

Figure 11.- Simplified block diagram of delta-wing flutter-suppression system.

the open-loop experimental studies, the control surfaces were kept at 0° deflection by applying hydraulic pressure to both control actuators. The pressurized system acted as a stiff spring to keep the rotational frequency of each control surface many times higher than the wing flutter frequency.

Modification

During the implementation of control laws B and C on the model, some difficulties were encountered. In effect, the system was so sensitive that if the model was disturbed in still air, the control surfaces would begin to oscillate and, in turn, drive the model in an unstable condition through the feedback loop. It is believed that this instability was due primarily to inertia coupling between the control surfaces and the wing. It was shown experimentally that this instability was driven by the rate feedback terms (that is, the values of gain in the [G] matrix, fig. 1). The difficulty was then cured by compromising the analytical values of the [G] matrix for control laws B and C. This was accomplished by experimentally varying the gains in the [G] matrix until the wind-off instability disappeared. For clarity, the control laws with modified [G] matrix gain values will be referred to hereafter as control law B Mod and control law C Mod.

An analytical study of these modified control laws was made to determine the effect that they would have on the energy eigenvalues and the predicted flutter dynamic pressure. As shown in figure 12, the effects of these modified gains on the energy eigenvalues appeared to be minimal aside from a reduction in the maximum positive values. However, the effect of these modified gains on the predicted flutter dynamic pressure was much

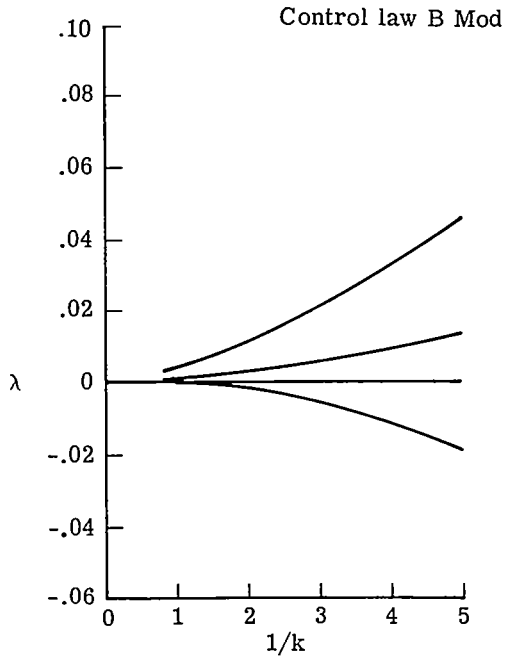

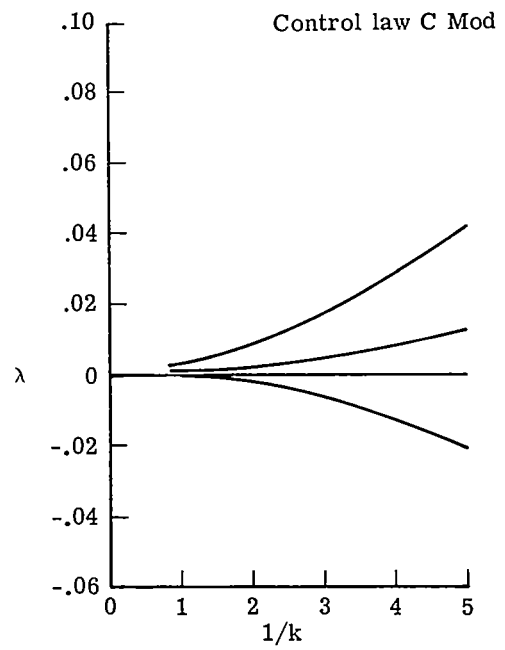

Figure 12.- Variation of λ with $1/k$ for modified control laws.

more pronounced. For example, the predicted flutter dynamic pressure for control law C Mod showed only 34-percent increase above the open-loop flutter dynamic pressure as compared with a 46.7-percent increase for the unmodified control law C. Considerably larger effects resulted in the predicted flutter dynamic pressure for control law B Mod which gave a 24-percent increase above the open-loop flutter dynamic pressure as compared with a 630 percent increase for the unmodified control law B. However, for the leading-edge and trailing-edge control case, it should be noted that control law B Mod still gave significantly larger calculated increase in flutter dynamic pressure than that for control law A. Since one of the purposes of the program was to verify analytical techniques, it was decided to implement and test control laws B Mod and C Mod. The gain values that were finally implemented on the model for control law B Mod and C Mod are given in table V.

TABLE V.- DELTA-WING MODEL CONTROL LAWS WITH COMPROMISED EXPERIMENTALLY TESTED VALUES

Control law A

$$\begin{Bmatrix} \beta \\ \delta \end{Bmatrix} = \begin{bmatrix} 0 & 5.6 \\ 0 & -1.4 \end{bmatrix} \begin{Bmatrix} h_1/b \\ \alpha \end{Bmatrix} + i \begin{bmatrix} 0 & 1.5 \\ 0.6 & 0.2 \end{bmatrix} \begin{Bmatrix} h_1/b \\ \alpha \end{Bmatrix}$$

Control law B Mod

$$\begin{Bmatrix} \beta \\ \delta \end{Bmatrix} = \begin{bmatrix} 0 & 0 \\ 2.7 & -5.3 \end{bmatrix} \begin{Bmatrix} h_1/b \\ \alpha \end{Bmatrix} + i \begin{bmatrix} 0 & 2.5 \\ 1.0 & 0.75 \end{bmatrix} \begin{Bmatrix} h_1/b \\ \alpha \end{Bmatrix}$$

Control law C Mod

$$\begin{Bmatrix} \beta \\ \delta \end{Bmatrix} = \begin{bmatrix} 0 & 0 \\ 2.7 & -5.3 \end{bmatrix} \begin{Bmatrix} h_1/b \\ \alpha \end{Bmatrix} + i \begin{bmatrix} 0 & 0 \\ 2.5 & 0.75 \end{bmatrix} \begin{Bmatrix} h_1/b \\ \alpha \end{Bmatrix}$$

WIND TUNNEL AND TEST PROCEDURES

Wind Tunnel

The investigation was conducted in the Langley transonic dynamics tunnel. This facility is specially designed for and almost totally dedicated to testing of dynamic aero-

elastic models. It is a closed-circuit continous-flow tunnel which has a 4.88-m square test section (with cropped corners) with slots in all four walls. It is capable of operation at stagnation pressures from near vacuum to slightly above atmospheric and at Mach numbers from near 0 to 1.2. Mach number and dynamic pressure can be varied simultaneously, or independently, with either air or Freon as a test medium. Freon was used for all tests of this investigation. The tunnel is equipped with four quick-opening bypass valves (hydraulic) which can be operated when flutter is encountered to reduce rapidly the dynamic pressure and Mach number in the test section. A more complete description of the wind tunnel is given in reference 36.

Test Procedure

The normal and most efficient tunnel operation procedure is to simply increase the motor fan speed and thereby increase both Mach number and dynamic pressure simultaneously along an approximately constant stagnation pressure line as shown in figure 13. This procedure of operation was used initially to define the basic-wing (open-loop) flutter boundary. However, a different procedure of operation was used for most of these tests because of the requirement to compare open-loop data with closed-loop data with a minimum number of variables involved. This different procedure consisted of holding Mach

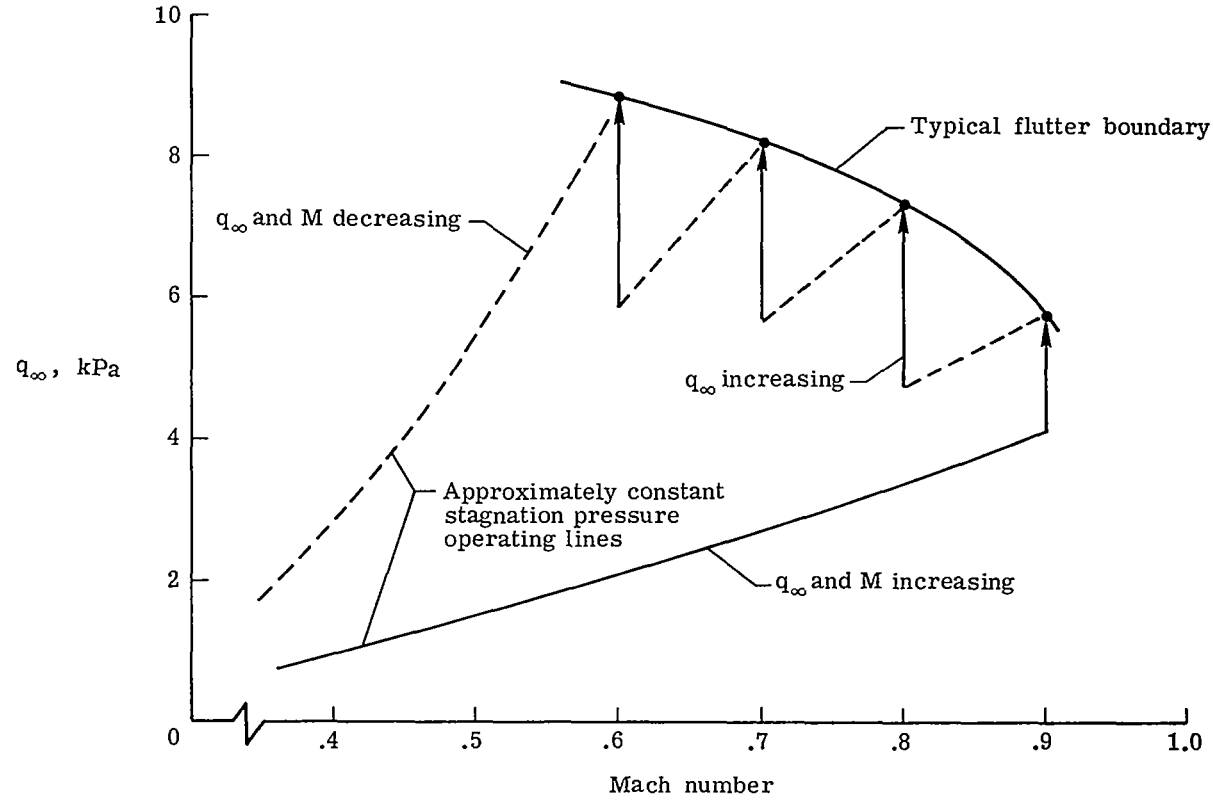

Figure 13.- Wind-tunnel operating procedure for this investigation.

number constant while increasing only dynamic pressure by continuously pumping Freon into the tunnel as shown by the arrows in figure 13. At selected points both Mach number and dynamic pressure were held constant while data (open-loop and closed-loop operation) were gathered and analyzed. At these data points below the flutter boundary, subcritical model response measurements were made to compare the open-loop and closed-loop model response. The primary variable measured was the damping of the model structural modes. Three subcritical response methods were used and are referred to as Co-Quad, Randomdec, and Peak-Hold Spectrum methods. Some results of all three methods are presented in the section "Results and Discussion," and a description of each method is presented in appendix C.

Data Gathering Procedure

During these tests, tunnel conditions were monitored and automatically recorded on punched cards and typewriter printouts. The model behavior was monitored visually at all times. Permanent visual records of the model behavior at selected points were provided by several high-speed motion picture cameras. Also, a closed-circuit television tape system was used to provide quick reviews of the flutter occurrences. All model instrumentation (such as strain gages, accelerometers, and solar cell position indicators) signals were recorded continuously on direct readout recorders and on magnetic tape.

RESULTS AND DISCUSSION

General

The experimental flutter studies of the delta-wing model were conducted in the Langley transonic dynamics tunnel at Mach numbers of 0.6, 0.7, 0.8, and 0.9. Open-loop flutter tests of the model were conducted first to establish the basic-wing flutter boundary. Then followed closed-loop tests of the model to evaluate the effect of active controls on raising the flutter boundary. These closed-loop tests included the evaluation of three different control laws A, B Mod, and C Mod. All experimental studies of control laws A and B Mod were restricted to a Mach number of 0.9 because of an unexplained high-frequency, large-amplitude oscillation of the leading-edge control surface. Since this phenomenon occurred with both open-loop (to a much lesser degree) and closed-loop operation and at a frequency of about 65 Hz, well above the flutter frequencies of 11 to 12.5 Hz, the problem is not believed to be a result of the control law. Also, this phenomenon was observed in time history records of actuator position during one test in which the leading-edge control surface was disengaged completely from the hydraulic actuator shaft. That is, the closed-loop system remained in operation, but without a control surface attached to the leading-edge hydraulic actuator. The phenomenon was of major concern throughout the investigation because it did limit the test objective because of increasing amplitudes with

increasing dynamic pressures. Many attempts were made to determine the exact cause but none were successful. By use of high-speed motion pictures and visual observation, it was determined that the flutter motion of the delta-wing model for the open-loop operation and that for the closed-loop operation were similar in nature and closely resembled the second natural vibration mode coupled with some primary bending. A summary of the experimental results is presented in table VI.

Flutter

Open-loop experimental results.- The experimental flutter characteristics for the delta-wing model are presented in figure 14 in terms of the variation of flutter-speed-index parameter with Mach number. The flutter boundary indicates a transonic drop in the flutter-speed index of about 15 percent from a Mach number of 0.6 to a Mach number of 0.9. Earlier model studies reported in reference 31 of an identical delta-wing planform show a similar drop along with a minimum flutter-speed-index value occurring at a Mach number of 0.92.

Closed-loop experimental results.- Each of the three control laws (A, B Mod, and C Mod) demonstrated increases in dynamic pressure above the open-loop flutter dynamic pressure at a Mach number of 0.9. For control law A the model fluttered at 12.5-percent

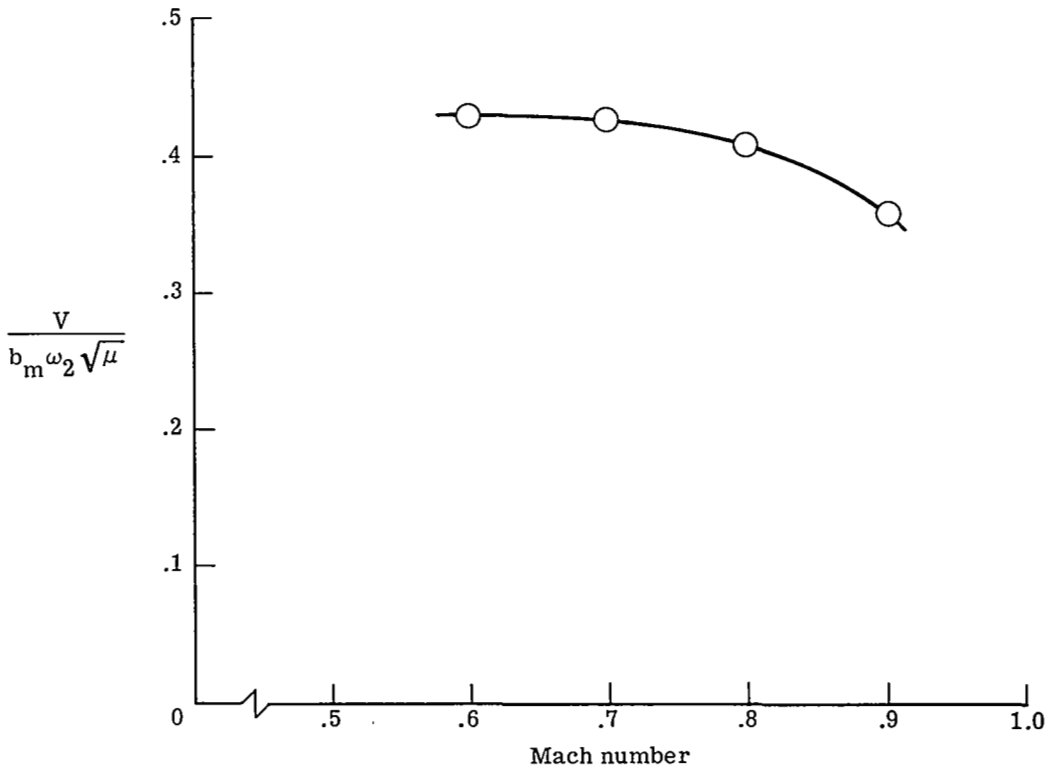

Figure 14.- Open-loop flutter characteristics of delta-wing model.

TABLE VI.- COMPILATION OF EXPERIMENTAL RESULTS

Control law	Mach number	Dynamic pressure, kPa	Velocity, m/s	Test medium density, kg/m^3	Reynolds number, m^{-1}	Flutter frequency, Hz	f_2, Hz	μ	$\frac{V}{b_m 2\pi f_2 \sqrt{\mu}}$
Open loop									
None	0.601	7.33[a]	93.0	1.695	12.19×10^6	12.4	15.4[a]	13.6	0.437
	.698	7.21[a]	106.6	1.269	10.65×10^6	12.1	15.4[a]	18.1	.434
	.799	7.42	123.3	.976	9.37×10^6	12.0	16.4	23.6	.413
	.904	5.88	138.9	.610	6.63×10^6	11.0	16.4	37.7	.368
Closed loop									
A	0.901	6.60	139.1	0.682	7.39×10^6	11.0	16.4	33.7	0.390
B Mod	0.895	7.15	140.5	0.724	7.70×10^6	No flutter	16.4	31.8	0.406
C Mod	0.606	8.13[a]	93.8	1.849	13.38×10^6	↓	15.4[a]	12.4	0.462
	.702	8.08[a]	108.5	1.373	11.55×10^6		15.4[a]	16.8	.459
	.802	8.89	124.0	1.156	11.13×10^6		16.4	19.9	.452
	.904	7.62	139.4	.784	8.52×10^6		16.4	29.4	.419

[a] Repaired model values. See page 34 for explanation of damage.

(These dynamic pressure values can be adjusted to compare with the undamaged model dynamic pressure values by use of the second-mode frequency ratio squared as follows:

$$(q_\infty)_{adj} = \left(\frac{16.4}{15.4}\right)^2 q_\infty = 1.134 q_\infty$$

The assumption is made that the model mass did not change.)

increase in dynamic pressure. Control law B Mod demonstrated a 22-percent increase in dynamic pressure. No flutter was encountered at this point; however, the test was terminated because of the leading-edge control surface instability discussed earlier. This result for control law B Mod represented a sizeable increase over that of control law A. Control law C Mod demonstrated a 30-percent increase in dynamic pressure (no flutter encountered). It should be noted that no definite conclusions should be drawn from these experimental closed-loop results as to the merits of leading-edge and trailing-edge active control systems compared with a trailing-edge active control system.

The effective operation of the flutter-suppression sytem is shown by the oscillograph trace of model response presented in figure 15. A typical time history of a bending strain gage with time increasing from left to right is shown in the figure. Open-loop flutter is shown on the left side, and closed-loop operation is shown on the right side. Note the increase in oscillatory amplitude until flutter begins and continues for about 4 seconds. At this point the flutter-suppression system (closed-loop) is turned on (indicated by the dashed line); its effect is seen almost immediately and the oscillatory flutter motion is damped rapidly. The degree of confidence in the closed-loop system was such that whenever open-loop flutter was encountered, the active control loop was closed to suppress the flutter motion. Or stating it another way, the flutter-suppression system was literally used as a "flutter stopper."

Comparison of analytical and experimental results.- A comparison of the calculated results for the three control laws with the aforementioned experimental results is presented in figure 16. The results are presented in terms of percent increase in dynamic pressure above the open-loop flutter dynamic pressure at a Mach number of 0.9. For control law A the calculated increase in flutter dynamic pressure shows very good agreement (within 1.0 percent) with the measured increase of 12.5 percent. Some earlier analytical results for control law A were reported in reference 28 which showed a 21-percent

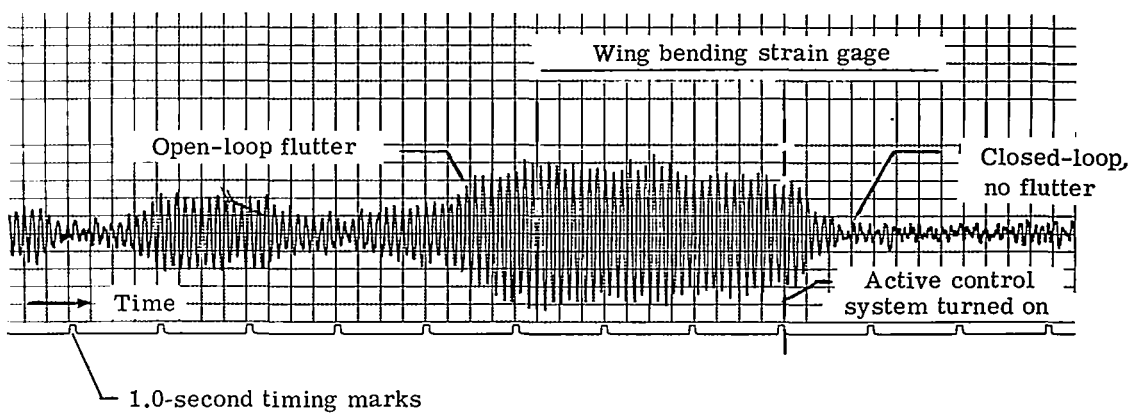

Figure 15.- Typical time history trace showing effective operation of delta-wing flutter-suppression system. Control law C Mod.

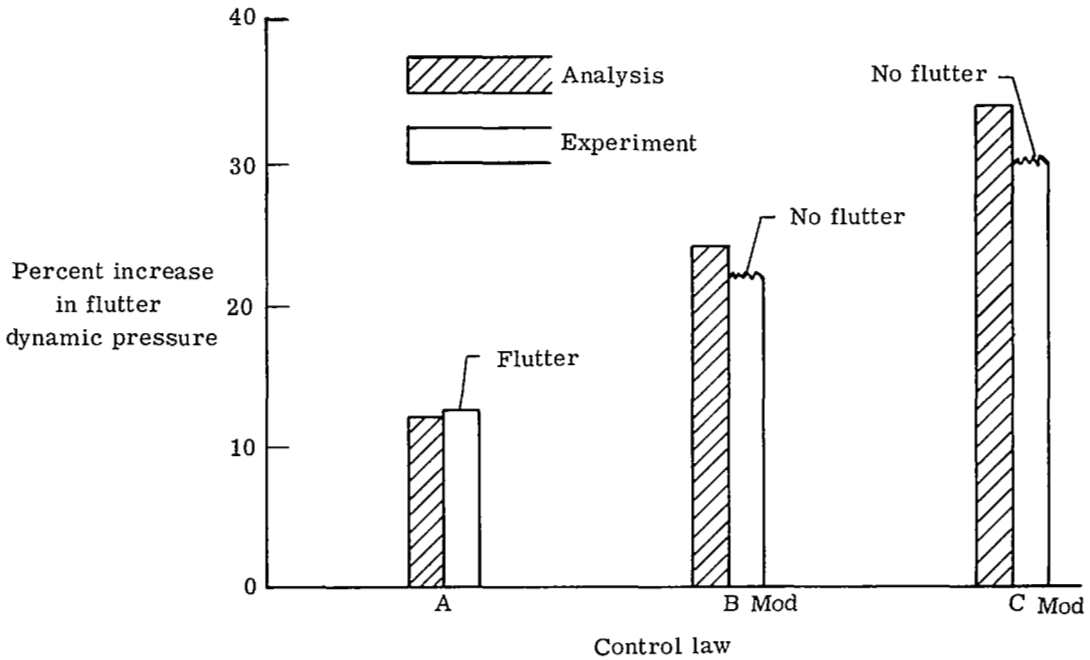

Figure 16.- Effect of different control laws on flutter dynamic pressure at M = 0.9.

increase. This difference is attributed to the fact that for the present analytical study the control surface aerodynamic forces were adjusted to take into account the differences between measured and calculated values of static hinge moments as discussed in appendix A. For control law B Mod the calculations predicted a 24-percent increase in dynamic pressure as compared with a measured no-flutter value of a minimum increase of 22 percent. For control law C Mod the calculations predicted a 34-percent increase in dynamic pressure as compared with a measured no-flutter value of a minimum increase of 30 percent. Of the three control laws investigated experimentally, control law C Mod exhibited the largest increase in dynamic pressure above the open-loop flutter dynamic pressure. It should be pointed out here that it is believed that a leading-edge and trailing-edge control law has the most potential to suppress flutter as Nissim stated in reference 24. Recall that based on analytical results, the original uncompromised control law B shows an increase in flutter dynamic pressure of over 600 percent above the open-loop flutter dynamic pressure.

These same analytical results are presented in figure 17 in a different, but familiar form of plots of damping against velocity (V-g plot). These V-g plots (for Mach number of 0.9) trace the first four wing modes and demonstrate the relatively violent nature of the flutter by the steep slope crossing of the zero damping line. The critical flutter mode for the open-loop basic wing and that for the closed-loop control law A are seen to be the first mode in figures 17(a) and 17(b), respectively. However, the critical flutter mode has

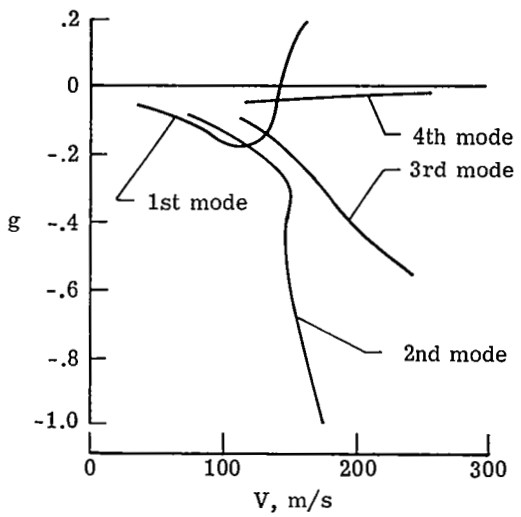

(a) Basic wing. V_f = 140.46 m/s.

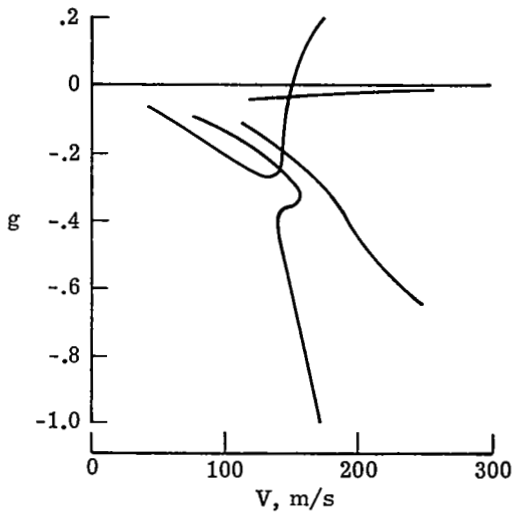

(b) Control law A. V_f = 148.84 m/s.

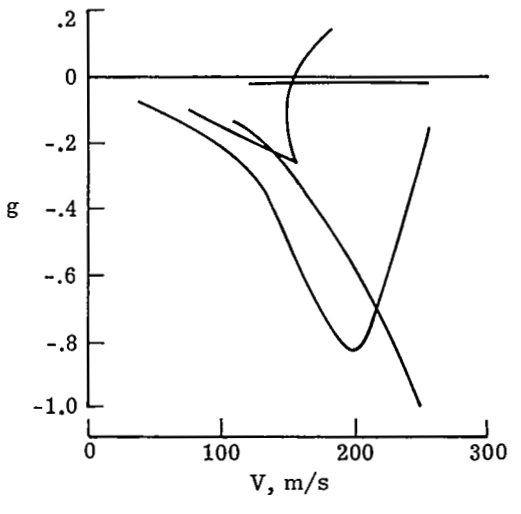

(c) Control law B Mod. V_f = 155.96 m/s.

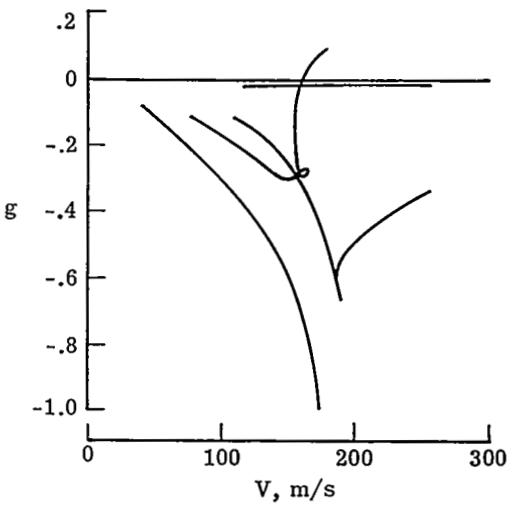

(d) Control law C Mod. V_f = 161.29 m/s.

Figure 17.- Variation of damping with velocity for M = 0.9 and ρ = 0.6713 kg/m^3.

switched to the second mode for control law B Mod and control law C Mod as shown in figures 17(c) and 17(d), respectively.

Mach number effects.- Additional studies were made to evaluate the active control system at other Mach numbers. These studies were limited to control law C Mod and included both experimental and analytical results for Mach numbers of 0.6, 0.7, 0.8, and 0.9. The results obtained are presented in figure 18 in terms of the variation of flutter-speed-index parameter with Mach number. The experimentally measured open-loop flutter boundary and the closed-loop no-flutter points for each Mach number are presented. At a Mach number of 0.8, a 9.4-percent increase in flutter-speed index (20 percent in dynamic pressure) is shown. Unfortunately, at this point the model was damaged owing to saturation of the closed-loop system because of the limited available actuator angle ($\pm 9^{o}$). Saturation caused the analog computer amplifiers to overload and forced the control surface to go hard against its stop; thus, open-loop flutter resulted. The model was repaired and tested at Mach numbers of 0.7 and 0.6 to demonstrate experimentally that the closed-loop system would not degrade the open-loop flutter characteristics. A modest increase in the flutter-speed index of 5.7 percent (12 percent in dynamic pressure) was demonstrated at these two Mach numbers. A comparison of open-loop experimental results (solid circle) with the open-loop analytical results (open square) in figure 18 shows reasonable agreement at all Mach numbers.

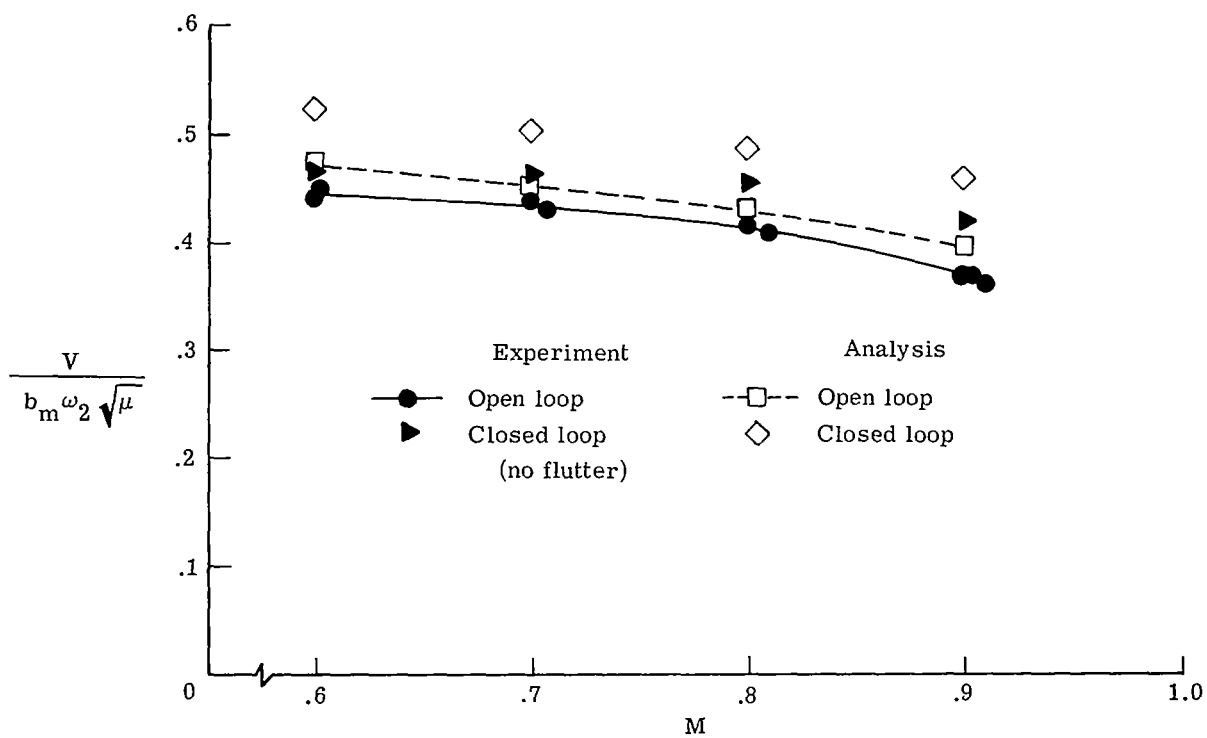

Figure 18.- Measured and calculated variation of flutter-speed-index parameter with Mach number. Control law C Mod.

Subcritical Response

To explore the behavior of the model below the flutter boundary (subcritical response), and to demonstrate the effectiveness of the flutter-suppression system, three different subcritical response methods were used and evaluated throughout this investigation. The methods are referred to as Co-Quad, Randomdec, and Peak-Hold Spectrum. A brief description of each method is given in appendix C.

Both Co-Quad and Randomdec methods were successfully used during the test as shown by the open-loop and closed-loop results in figure 19. The results are presented in terms of the stability criteria damping plotted against dynamic pressure. These two subcritical response methods were quite helpful during the test in that they did forecast the approach to flutter and showed that the flutter-suppression system was working effectively by the sizable damping increase obtained between open-loop and closed-loop operation at a given dynamic pressure. In figure 19 the symbols represent the actual measured damping values obtained by using the two methods.

The Peak-Hold Spectrum method was not used during on-line tests but was applied in post-test analysis of the experimental data. Instead of damping, this method uses the inverse model response as the stability criteria. The peak-hold method is similiar to a subcritical response method described in reference 37. For the mode of interest, the inverse amplitude is obtained from a "peak-hold" spectrum (using special electronic equipment) and is plotted against dynamic pressure as shown in figure 20. Results for both

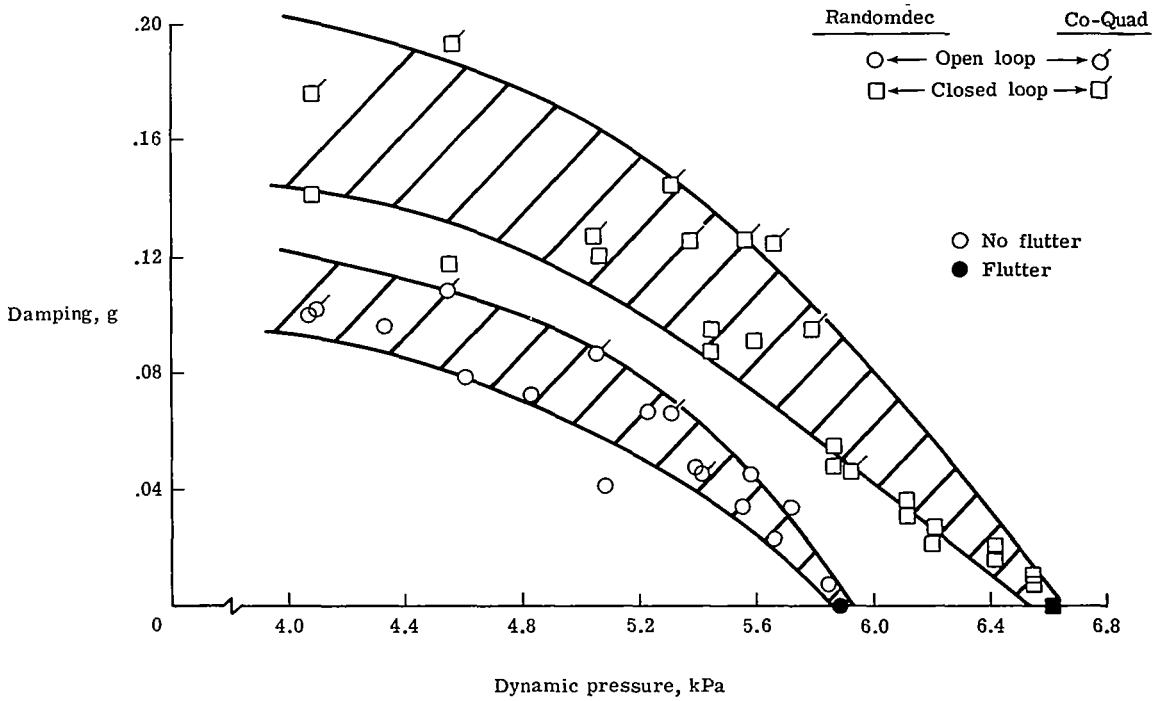

Figure 19.- Measured subcritical damping at Mach number of 0.9.

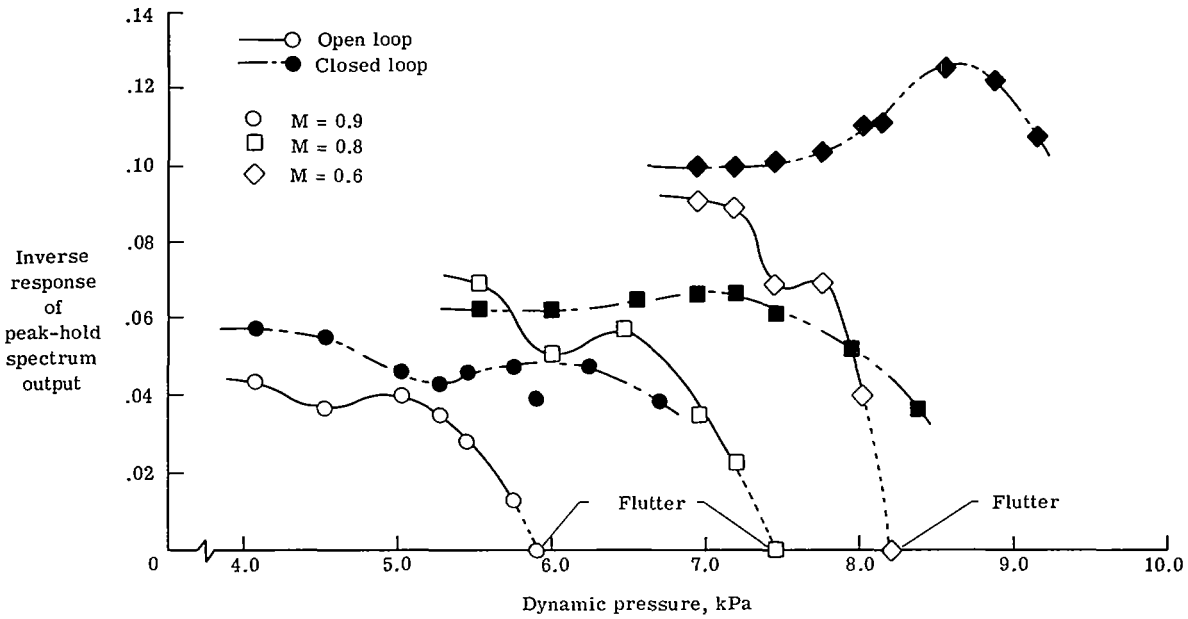

Figure 20.- Forced subcritical response data using Peak-Hold Spectrum method.

open-loop and closed-loop subcritical response data are presented in figure 20 for three different values of Mach number. Of the three different subcritical response methods used and evaluated in this flutter study, the Peak-Hold Spectrum method, in general, gave the most consistent results.

A comparison of calculated and measured subcritical response data obtained by using the Co-Quad method is presented in figure 21 for a Mach number of 0.9. Both the in-phase and out-of-phase response of the model are shown in terms of the ratio of accelerometer output $\ddot{h}_1$ to trailing-edge command signal $\delta_{t,c}$. The curves on the right-hand side of figure 21 represent closed-loop operation (control law C Mod) at the open-loop flutter dynamic pressure. A comparison between the open-loop and closed-loop response peak amplitudes at the flutter frequency near 11 Hz demonstrates the effectiveness of active controls to suppress flutter. The analysis agrees well with the measured response except for the open-loop out-of-phase response peak amplitude value near 11 Hz.

CONCLUSIONS

Experimental and analytical studies to evaluate active control flutter-suppression systems based on an aerodynamic energy method have been described. A simplified delta-wing model was used and three different control laws were investigated. Control law A used both leading-edge and trailing-edge control surfaces and was formulated by using two-dimensional unsteady aerodynamic theory. Control law B Mod differed from control law A in that three-dimensional unsteady aerodynamics were used. Control law C Mod

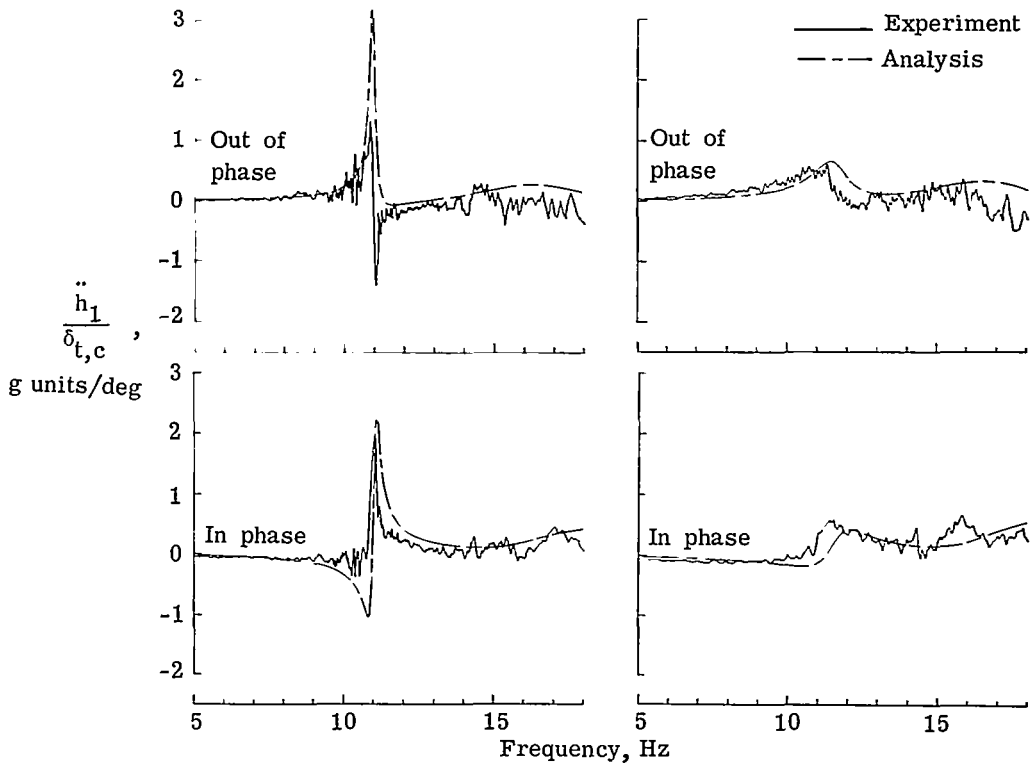

(a) Open loop (q_∞ = 0.95 open-loop flutter).

(b) Closed loop (q_∞ = 1.0 open-loop flutter).

Figure 21.- A comparison of measured and calculated forced response to trailing-edge-control excitation at M = 0.9.

used only a trailing-edge control surface and was formulated by using three-dimensional unsteady aerodynamic theory. Some important results were accomplished and are listed as follows:

1. An active flutter-suppression system was demonstrated successfully with the use of active leading-edge and trailing-edge control surfaces to suppress flutter on the model in the wind tunnel.

2. An aerodynamic energy concept for flutter suppression was validated experimentally by using three different control laws. The closed-loop results at a Mach number of 0.9 demonstrated an increase in dynamic pressure above the open-loop flutter dynamic pressure of 12.5 percent for control law A, a minimum of 22 percent for control law B Mod, and a minimum of 30 percent for control law C Mod. Note that no flutter was encountered with control laws B Mod and C Mod.

3. Analytical studies based on three-dimensional aerodynamic theory indicated that a leading-edge and trailing-edge control law is potentially better than a trailing-edge control law.

4. Some major advances in modeling technology were made in the development of miniature hydraulic actuators and small reliable solar cell position sensors.

5. The control law equations were implemented successfully on an analog computer.

6. A flutter analysis employing doublet-lattice aerodynamics was used to predict both open-loop and closed-loop flutter results. The open-loop flutter analysis results agreed well with the corresponding experimental flutter results for Mach numbers of 0.6, 0.7, 0.8, and 0.9. Also, the closed-loop flutter analysis results showed good agreement with the only experimental closed-loop flutter point obtained (for control law A at Mach number of 0.9) in this investigation.

7. Subcritical response methods proved useful in forecasting the approach to flutter and in evaluating the effectiveness of the flutter-suppression system. Three different subcritical response methods, called Co-Quad, Randomdec, and Peak-Hold Spectrum methods, were used and evaluated in this investigation. The Peak-Hold Spectrum method, in general, gave the best results.

8. Analytically predicted forced subcritical response data agreed reasonably well with the corresponding measured subcritical response data obtained by using the Co-Quad method.

Langley Research Center
National Aeronautics and Space Administration
Hampton, Va. 23665
November 6, 1975

APPENDIX A

AEROELASTIC ANALYSIS

A detailed analysis used to calculate the flutter characteristics, both with and without active controls, is developed in this appendix. Also included is a discussion of quantitative procedures used to correct, for use in the analysis, the theoretical unsteady pressures due to control surface motion.

Equations of Motion

The equations of motion are formulated through a modal approach involving the use of Lagrange's equations of motion. In the modal approach the elastic deformation at any point on the wing is described by a linear combination of orthogonal modes, that is, the undamped natural modes of the system, in the following manner:

$$h(x,y,t) = \sum_{i=1}^{n} q_i(t)\, Z_i(x,y) \tag{A1}$$

If structural damping and control surface dynamics are neglected, Lagrange's equations of motion for the system become

$$M_i\ddot{q}_i(t) + \omega_i^2 M_i q_i(t) = Q_i(t) \qquad (i = 1, 2, 3, \ldots, n) \tag{A2}$$

where

$$M_i = \iint_S m(x,y)\, Z_i^2(x,y)\, dx\, dy$$

is the generalized mass and

$$Q_i(t) = \iint_S \Delta p(x,y,t)\, Z_i(x,y)\, dx\, dy$$

is the generalized aerodynamic force. If motions of small amplitude are assumed, the total-pressure distribution $\Delta p(x,y,t)$ may be expressed as the sum of contributions due to each flexible mode plus those due to the leading-edge and trailing-edge controls. Therefore,

$$\Delta p(x,y,t) = \sum_{j=1}^{n} \Delta p_j(x,y)\, q_j(t) + \Delta p_\delta(x,y)\, \delta(t) + \Delta p_\beta(x,y)\, \beta(t)$$

where $\Delta p_j(x,y)$ is the lifting pressure at point x,y due to motion of the wing in the jth flexible mode, and $\Delta p_\beta(x,y)$ and $\Delta p_\delta(x,y)$ are the pressures due to leading-edge and trailing-edge controls, respectively. Substituting this expression for the pressures into equation (A2) and expanding results in the following form of the equations of motion:

$$M_i \ddot{q}_i(t) + \omega_i{}^2 M_i q_i(t) = \sum_{j=1}^{n} \left[q_j(t) \iint_S \Delta p_j(x,y)\, Z_i(x,y)\, dx\, dy \right] + \beta(t) \iint_S \Delta p_\beta(x,y)\, Z_i(x,y)\, dx\, dy$$

$$+ \delta(t) \iint_S \Delta p_\delta(x,y)\, Z_i(x,y)\, dx\, dy \qquad (i = 1, 2, 3, \ldots, n) \qquad \text{(A3)}$$

Control Law Relationships

The basic control law which relates control surface deflections to the wing motion is of the form

$$\begin{Bmatrix} \beta \\ \delta \end{Bmatrix} = \begin{bmatrix} C_{11} & C_{12} \\ C_{21} & C_{22} \end{bmatrix} \begin{Bmatrix} h_1/b \\ \alpha \end{Bmatrix} + i \begin{bmatrix} G_{11} & G_{12} \\ G_{21} & G_{22} \end{bmatrix} \begin{Bmatrix} h_1/b \\ \alpha \end{Bmatrix} \qquad \text{(A4)}$$

where h_1 and α are the plunging and pitching motions, respectively, of a representative section of the wing. The pitching motion is determined by measuring the response of the wing at two points along a representative section as indicated in the following sketch:

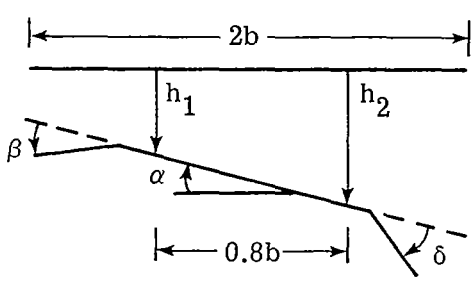

From equation (A1), the nondimensional deflection for h_1 and h_2 can be written as

$$\frac{h_1}{b} = \frac{h(x_1,y_1)}{b} = \frac{1}{b}\sum_{i=1}^{n} q_i(t)\, Z_i(x_1,y_1)$$

$$\frac{h_2}{b} = \frac{h(x_2,y_1)}{b} = \frac{1}{b}\sum_{i=1}^{n} q_i(t)\, Z_i(x_2,y_1)$$

Assuming that a straight line between the locations x_1 and x_2 gives a reasonable approximation to the angle of attack of the reference station and noting that the sensors[1] are 0.8b apart leads to the following equation for the angle of attack α:

$$\alpha = \frac{h_2 - h_1}{0.8b} = \frac{1}{0.8b}\sum_{i=1}^{n} \left[Z_i(x_2,y_1) - Z_i(x_1,y_1)\right] q_i(t)$$

Substituting these results into the control law equation (A4) results in a matrix equation relating the control surface motions to the generalized coordinates of the system in the following form:

$$\begin{Bmatrix} \beta \\ \delta \end{Bmatrix} = \begin{bmatrix} A_1 + iB_1 & A_2 + iB_2 & \cdots & A_n + iB_n \\ C_1 + iD_1 & C_2 + iD_2 & \cdots & C_n + iD_n \end{bmatrix} \begin{Bmatrix} q_1 \\ q_2 \\ \cdot \\ \cdot \\ \cdot \\ q_n \end{Bmatrix} \tag{A5}$$

where the terms A_i, B_i, C_i, and D_i are constant coefficients defined as follows:

$$A_i = Z_i(x_1,y_1)\left(\frac{C_{11}}{b} - \frac{C_{12}}{0.8b}\right) + Z_i(x_2,y_1)\frac{C_{12}}{0.8b}$$

[1]It was found to be impractical to locate the two sensors exactly 0.8b apart because of the internal structure of the model. The actual location of each sensor is given in figure 4 and these values are used in all subsequent flutter analyses of the model in place of the 0.8b value.

$$B_i = Z_i(x_1,y_1)\left(\frac{G_{11}}{b} - \frac{G_{12}}{0.8b}\right) + Z_i(x_2,y_1)\frac{G_{12}}{0.8b}$$

$$C_i = Z_i(x_1,y_1)\left(\frac{C_{21}}{b} - \frac{C_{22}}{0.8b}\right) + Z_i(x_2,y_1)\frac{C_{22}}{0.8b}$$

$$D_i = Z_i(x_1,y_1)\left(\frac{G_{21}}{b} - \frac{G_{22}}{0.8b}\right) + Z_i(x_2,y_1)\frac{G_{22}}{0.8b}$$

Flutter Equations

Assuming oscillating motion and substituting equation (A5) into equation (A3) results in the following form of the equations of motion:

$$\left(-\omega^2 M_i + \omega_i{}^2 M_i\right)q_i = \sum_{j=1}^{n} q_j\left[\iint_S \Delta p_j(x,y)\, Z_i(x,y)\, dx\, dy + \left(A_j + iB_j\right)\iint_S \Delta p_\beta(x,y)\, Z_i(x,y)\, dx\, dy\right.$$

$$\left. + \left(C_j + iD_j\right)\iint_S \Delta p_\delta(x,y)\, Z_i(x,y)\, dx\, dy\right] \qquad (i = 1, 2, 3, \ldots, n) \qquad (A6)$$

In order to solve the preceding equations for the flutter characteristics, the following procedures are used. By letting

$$\left.\begin{aligned} \tfrac{1}{2}\rho V^2 A_{ij} &= \iint_S \Delta p_j(x,y)\, Z_i(x,y)\, dx\, dy \\ \tfrac{1}{2}\rho V^2 A_{i\beta} &= \iint_S \Delta p_\beta(x,y)\, Z_i(x,y)\, dx\, dy \\ \tfrac{1}{2}\rho V^2 A_{i\delta} &= \iint_S \Delta p_\delta(x,y)\, Z_i(x,y)\, dx\, dy \end{aligned}\right\} \qquad (A7)$$

equation (A6) becomes

$$\left(\frac{\omega_i^2}{\omega^2} - 1\right)\omega^2 M_i q_i = \frac{1}{2}\rho V^2 \sum_{j=1}^{n} q_j\left[A_{ij} + \left(A_j + iB_j\right)A_{i\beta} + \left(C_j + iD_j\right)A_{i\delta}\right] \qquad (i = 1, 2, 3, \ldots, n)$$

The equations of motion may now be written as

$$\sum_{j=1}^{n}\left[A_{ij} + \left(A_j + iB_j\right)A_{i\beta} + \left(C_j + iD_j\right)A_{i\delta} + \left(1 - \frac{\omega_j^2}{\omega_r^2}\Omega_r\right)\frac{2k^2 M_j \delta_{ij}}{\rho b_r^2}\right]q_j = 0 \qquad (i = 1, 2, 3, \ldots, n) \tag{A8}$$

Equation (A8) is homogeneous in the n generalized coordinates so that a nontrivial solution exists if, and only if, the determinant of the coefficients vanishes. At a constant Mach number the equations are solved for the neutral stability condition by treating the reduced frequency k as an input quantity, since the aerodynamic terms are functions of k and Mach number, and solving for the dependent variable Ω_r. These results can then be presented in the classical V-g manner as shown in figure 17, since

$$\Omega_r = \frac{\omega_r^2}{\omega^2}(1 + ig) = X + iY$$

where X and Y are the real and imaginery parts of Ω_r and

$$g = \frac{Y}{X}$$

$$V = \frac{b_r \omega_r}{k\sqrt{X}}$$

The neutral stability point corresponds to $g = 0$.

It should be noted from the form of equation (A8) that the active controls serve only to modify the aerodynamic forces of the wing. Flutter calculations without active controls are performed by setting the coefficients A_i, B_i, C_i, and D_i equal to zero.

APPENDIX A

Aerodynamic and Structural Properties

The solution of equation (A8) required that the physical properties of the model be described by a set of generalized masses, mode shapes, and natural frequencies. These properties were determined experimentally as described in the text under "Model Physical Properties." The mode shapes were measured at the model control points as shown in figure 22.

The aerodynamic terms appearing in equation (A8) were developed with the use of doublet-lattice aerodynamics by a numerical method similar to that presented in reference 38. In order to calculate the pressure distributions on an oscillating wing, the lifting surface is subdivided into an array of trapezoidal boxes arranged in strips parallel to the airstream as shown in figure 23. The lifting surface is then represented by a lattice of doublets located along the quarter-chord of each box. The downwash boundary condition is satisfied at the three-quarter chord of each box by equating the downwash to the slope and deflection of each structural mode. For all the calculations presented in this paper the lifting surface was divided into 160 boxes. The boxes were arranged in 16 streamwise strips with 10 boxes per strip. Figure 23 shows the aerodynamic paneling scheme and gives the location of the box edges in terms of the nondimensional wing span η and the local streamwise chord station x/c. Since the structural modes are not measured at the same points as required by the aerodynamic program, extensive use of natural cubic splines, similar to those described in reference 39, was made to determine the required slopes and deflections. The boxes used to represent the control surfaces are also shown in figure 23. It is assumed that the control surface edges are sealed.

Control Surface Aerodynamic Correction

During preliminary analytical investigations it was learned that large differences in the effectiveness of the active control system could be directly attributed to the accuracy in predicting the control surface aerodynamics. A comparison between calculated and measured static hinge moments is presented in figure 24. Because of the relatively small size of the controls with respect to the lifting surface and the inability of potential theory to predict detailed aerodynamic behavior associated with the controls, the lack of agreement is not surprising. It was decided therefore that all calculations should try to account for these differences in some empirical manner. Since unsteady hinge moments were not measured, the calculated unsteady control surface aerodynamic terms were adjusted by the ratio of measured to calculated static hinge moments. That is, aerodynamic terms appearing in equation (A3) of the form

$$\iint_S \Delta p_\delta(x,y)\, Z_i(x,y)\, dx\, dy$$

APPENDIX A

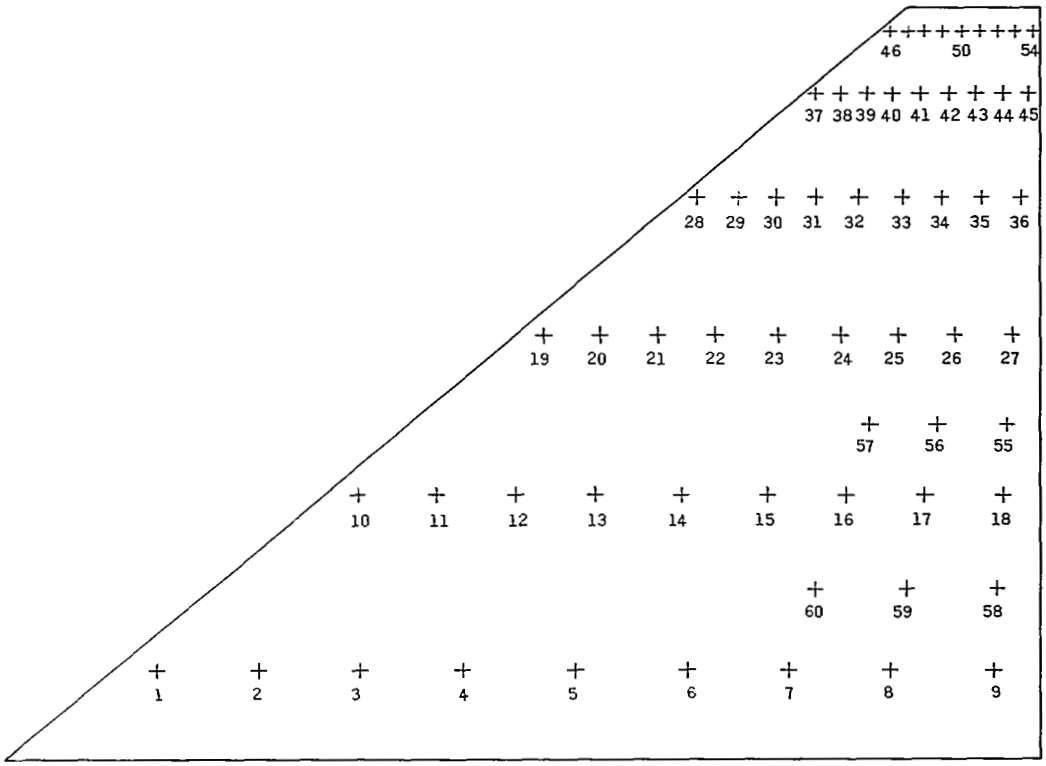

Pt	η	x/c	Pt	η	x/c	Pt	η	x/c	Pt	η	x/c	Pt	η	x/c	Pt	η	x/c
1	.1205	.05	10	.3546	.05	19	.5681	.05	28	.7485	.05	37	.8854	.05	46	.9709	.05
2	.1205	.16	11	.3546	.16	20	.5681	.16	29	.7485	.16	38	.8854	.16	47	.9709	.16
3	.1205	.27	12	.3546	.27	21	.5681	.27	30	.7485	.27	39	.8854	.27	48	.9709	.27
4	.1205	.38	13	.3546	.38	22	.5681	.38	31	.7485	.38	40	.8854	.38	49	.9709	.38
5	.1205	.50	14	.3546	.50	23	.5681	.50	32	.7485	.50	41	.8854	.50	50	.9709	.50
6	.1205	.62	15	.3546	.62	24	.5681	.62	33	.7485	.62	42	.8854	.62	51	.9709	.62
7	.1205	.73	16	.3546	.73	25	.5681	.73	34	.7485	.73	43	.8854	.73	52	.9709	.73
8	.1205	.84	17	.3546	.84	26	.5681	.84	35	.7485	.84	44	.8854	.84	53	.9709	.84
9	.1205	.95	18	.3546	.95	27	.5681	.95	36	.7485	.95	45	.8854	.95	54	.9709	.95

Pt[1]	η	x/c	Pt[1]	η	x/c
55	.4470	.95	58	.2290	.95
56	.4470	.84	59	.2290	.84
57	.4470	.73	60	.2290	.73

[1]Points 55 to 60 were added to define the nacelle motion for modes 3 to 9.

Figure 22.- Model control points for vibration test. Pt denotes point.

APPENDIX A

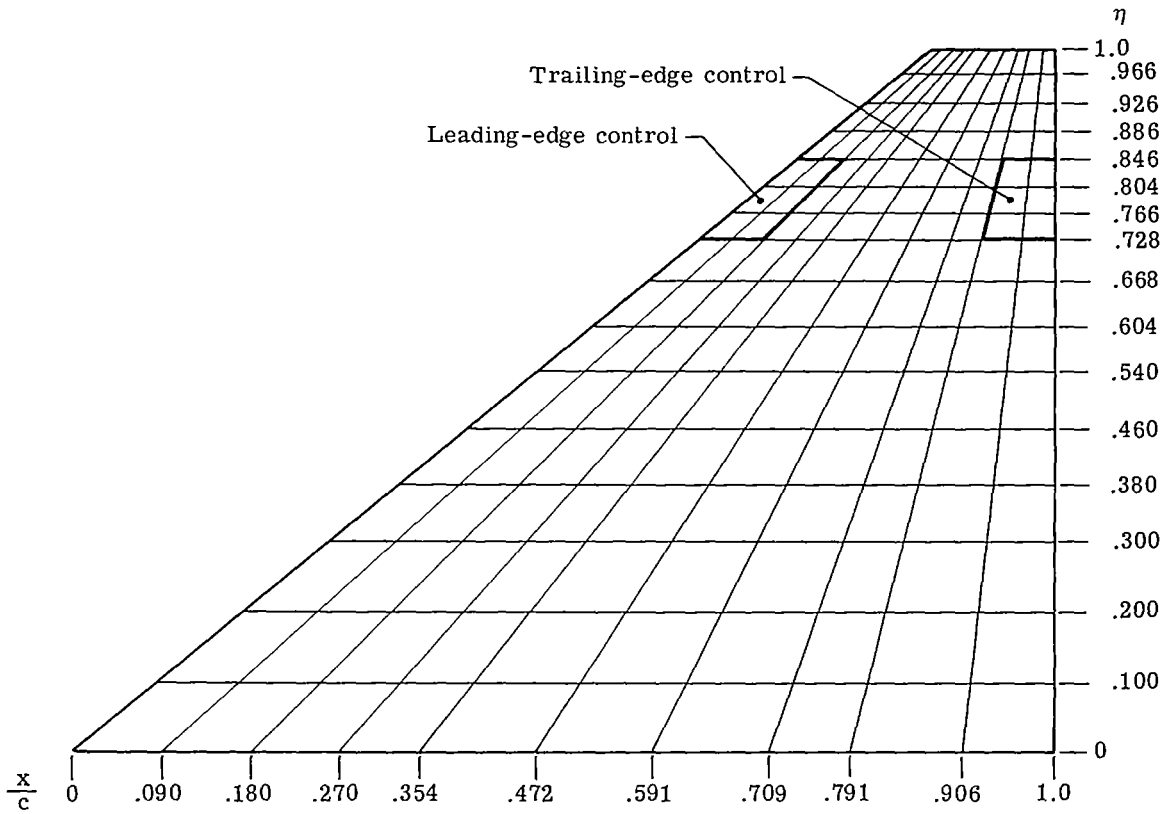

Figure 23.- Paneling scheme for doublet-lattice aerodynamics.

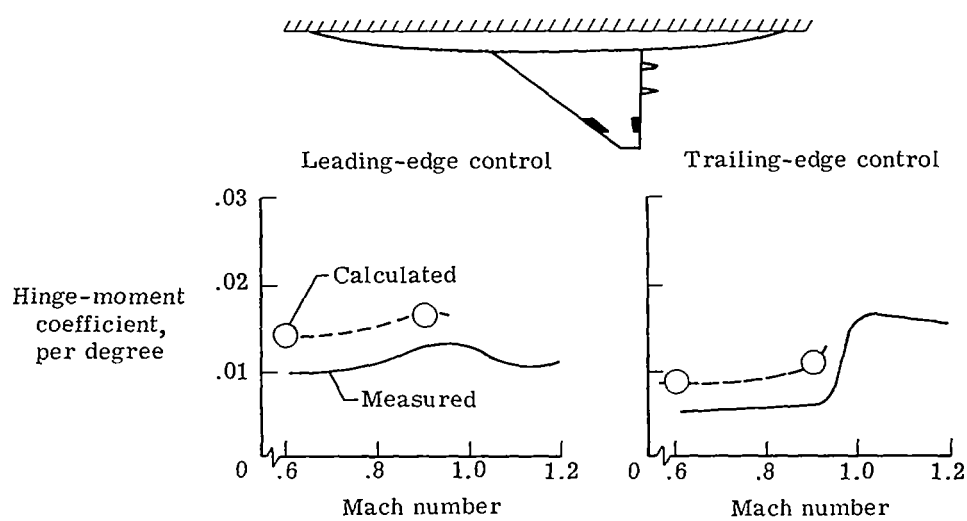

Figure 24.- Comparison of measured and calculated static hinge-moment coefficients.

and

$$\iint_S \Delta p_\beta(x,y)\, Z_i(x,y)\, dx\, dy$$

were multiplied by this factor before being used in the calculations. All calculations presented in this paper use this empirical correction factor.

APPENDIX B

FLUTTER-SUPPRESSION SYSTEM MECHANIZATION

Introduction

A brief description of the design and operation of the actuator loops and control law feedback loops is given in this appendix. The flutter-suppression control system (fig. 25) consists of leading-edge and trailing-edge control surfaces, control surface actuator loops, and control law feedback loops for each surface. The actuator loops are electrohydraulic position feedback systems which serve two functions: For zero command inputs, they maintain a fixed control surface position relative to the wing; and for time-varying inputs, they provide a control surface dyanmic response with the desired gain and phase characteristics. The control law feedback loops establish a specific relationship between control surface deflection and wing motion. This relationship is determined by the control law equations which are programed on an analog computer.

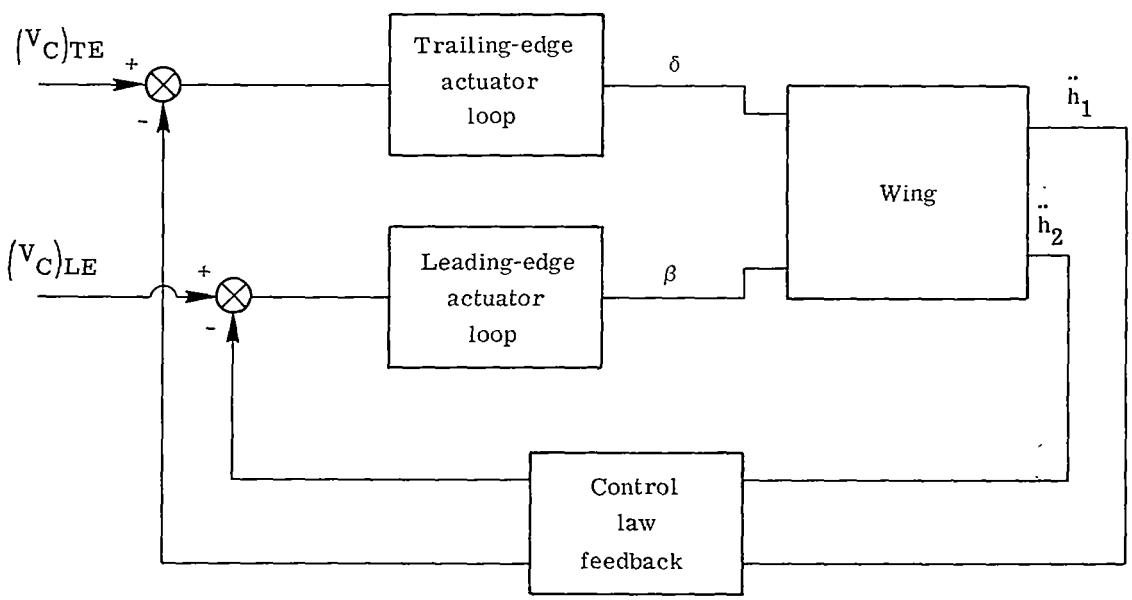

Figure 25.- Block diagram of the flutter-suppression system.

Actuator Loops

The actuator loops must be capable of displacing the control surfaces in the exact manner dictated by the control law over the operating frequency range. They also must prevent the control surfaces from being deflected relative to the wing by wind loads. These demands can be described in terms of actuator loop requirements as follows:

APPENDIX B

(1) The bandwidth of the actuator loops must be sufficiently wide relative to the flutter-suppression system operating frequency range to minimize amplitude variation and phase shift with respect to frequency.

(2) The actuators must have sufficient amplitude capability.

(3) The actuators must provide sufficient torque to drive the control surfaces under all operating conditions.

The first requirement is perhaps the most difficult to satisfy because, for the higher frequencies normally associated with flutter, a very wide actuator loop bandwidth is required.

Figure 26 is a diagram of the trailing-edge actuator loop. Since leading-edge and trailing-edge loops are very similar, only the trailing-edge loop is discussed. By ignoring the load pressure feedback for the moment, the operation of the loop can be described in the following manner. A command voltage V_{CA} is applied to the summing point where it is compared with a voltage V_δ proportional to the present position of the control surface. The difference between V_{CA} and V_δ generates a current input I_V to the servovalve through the servovalve amplifier. The servovalve provides a fluid flow to the actuator proportional to I_V and causes displacement of the control surface. The surface continues to move until the difference between V_{CA} and V_δ is essentially zero. The load pressure feedback through the high pass filter is used to stabilize the closed loop. The high pass filter removes the static and low-frequency components of the pressure signal.

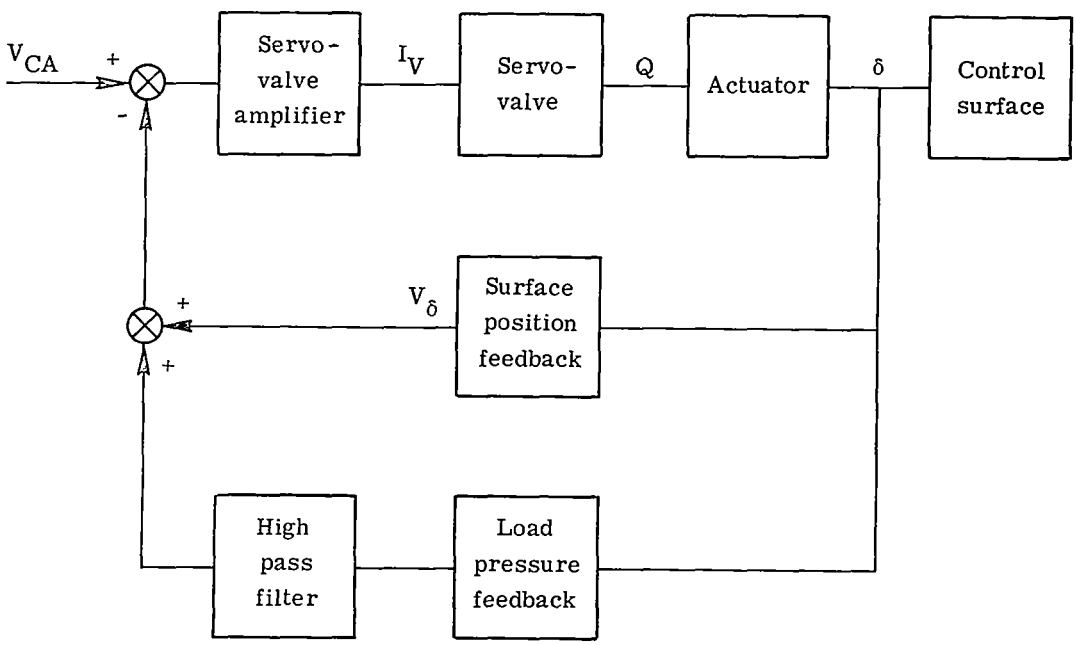

Figure 26.- Block diagram of the trailing-edge actuator loop.

APPENDIX B

A simplified mathematical model of the trailing-edge actuator loop which is derived in references 26 and 27 is shown in block diagram form in figure 27. This model was used to predict the behavior of the closed-loop system as a function of different system parameters.

The measured closed-loop frequency response of the trailing-edge actuator loop is shown in figure 28 for a 2° input command. In the operating frequency range of 4 Hz to 25 Hz, the amplitude is flat within $\pm 0.2^{\circ}$, and the phase shift does not exceed 27° lag. The damping of the dominant mode of the actuator loop was set by observing the control surface overshoot for a step input command. An overshoot of 37.2 percent, which corresponds to a relative damping of 0.3 for a second-order system, was set by adjusting the pressure feedback gain. The system deadband from the hysteresis plot of figure 29 was 0.2°. The leading-edge actuator loop characteristics were similar to the trailing edge.

Control Law Feedback Loops

The control law feedbacks establish the relationship between control surface deflection and wing response by means of the control law equations. These equations are programed on an analog computer and modify response signals from transducers on the model. These modified signals are inputs to the actuator loops which drive the control surfaces. The following describes how the control law equations were programed and discusses the circuitry needed to implement certain parts of these equations. Control law B Mod for leading-edge and trailing-edge control surfaces had the following form:

$$\begin{Bmatrix} \beta \\ \delta \end{Bmatrix} = \begin{bmatrix} 0 & 0 \\ C_{21} & C_{22} \end{bmatrix} \begin{Bmatrix} h_1/b \\ \alpha \end{Bmatrix} + i \begin{bmatrix} 0 & G_{12} \\ G_{21} & G_{22} \end{bmatrix} \begin{Bmatrix} h_1/b \\ \alpha \end{Bmatrix}$$

where β is the leading-edge control surface deflection; δ is the trailing-edge control surface deflection; h_1 and α are the plunging and pitching motions, respectively, of a representative streamwise section of the wing; b is a reference length; and C_{ij} and G_{ij} are constant coefficients. By referring to the sketch below,

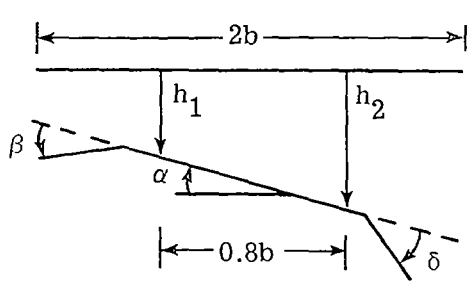

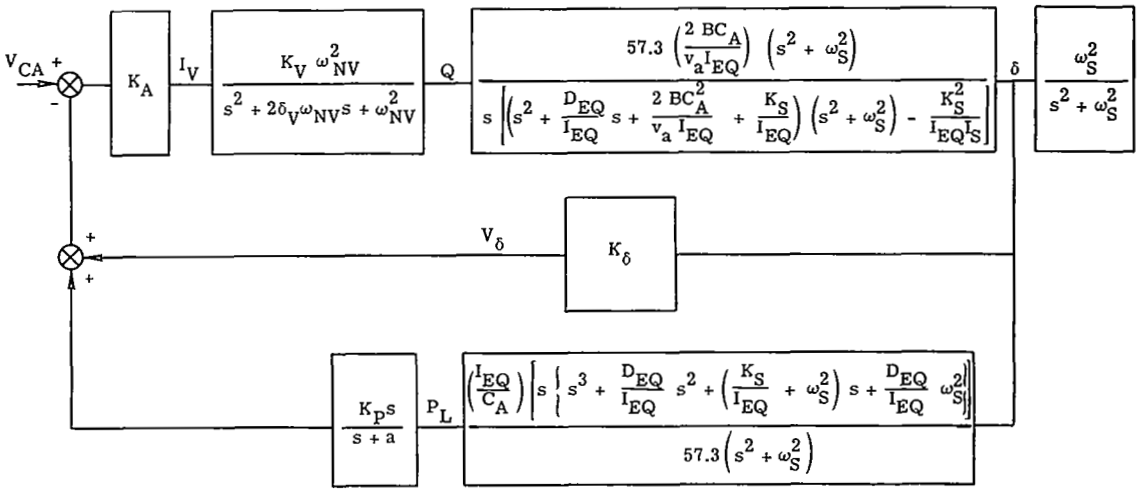

Figure 27.- Mathematical model of trailing-edge actuator loop.

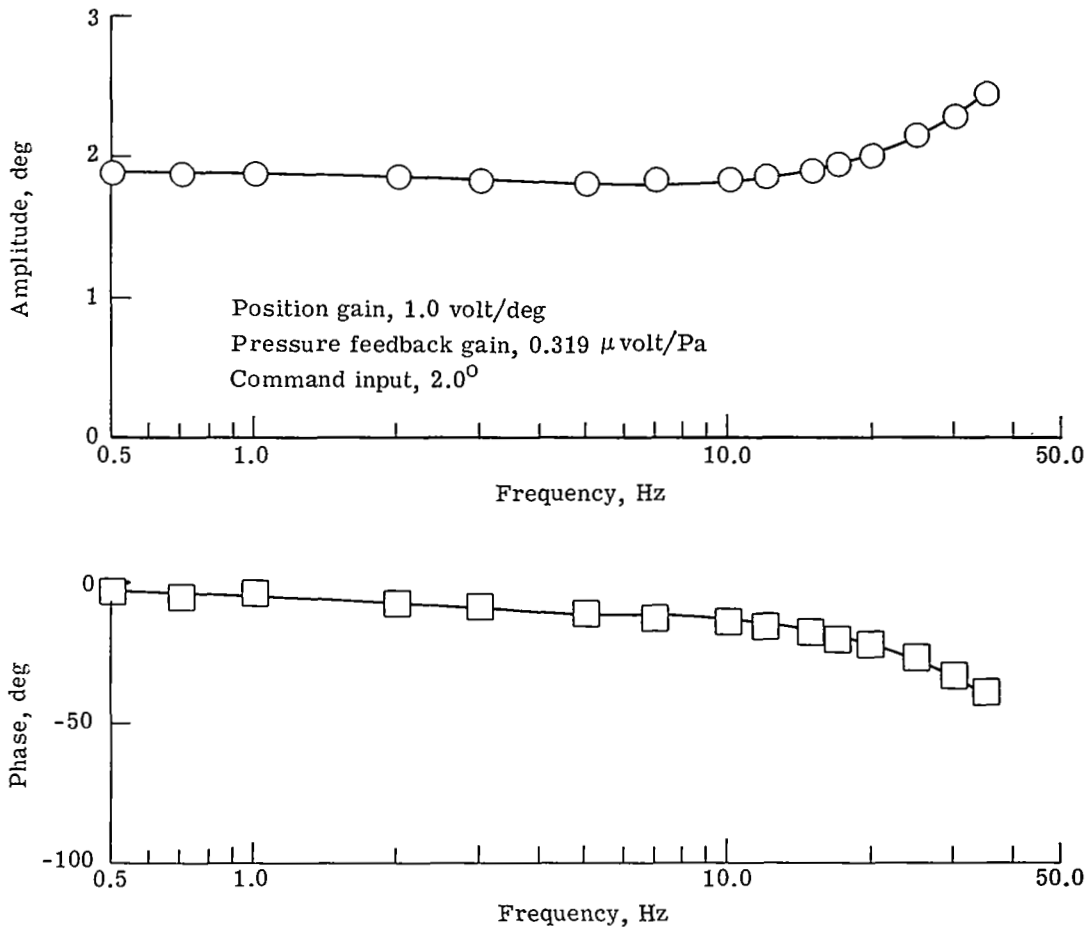

Figure 28.- Frequency response of trailing-edge actuator loop.

APPENDIX B

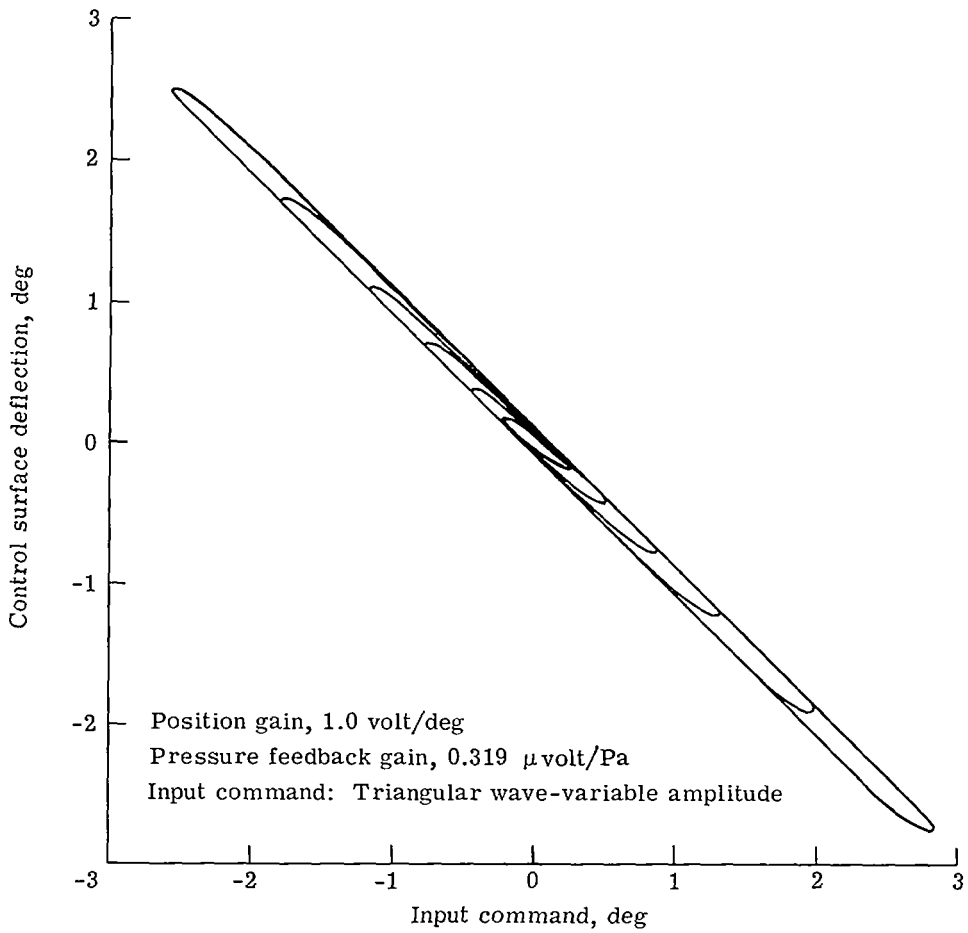

Figure 29.- Hysteresis plot of trailing-edge actuator loop.

the following sign conventions were used: β, positive when leading edge is down; δ, positive when trailing edge is down; h_1 and h_2, positive downward; and α, positive when leading edge is up where α is defined as $\alpha = (h_2 - h_1)/0.8b$.

If the control law matrix equation is expanded and the substitutions $ih = \dot{h}/\omega$ and $\alpha = (h_2 - h_1)/0.8b$ are made,

$$\hat{\beta} = \frac{57.3G_{12}}{0.8b}\frac{1}{\omega}\dot{h}_2 - \frac{57.3G_{12}}{0.8b}\frac{1}{\omega}\dot{h}_1 \tag{B1}$$

$$\hat{\delta} = 57.3\left(\frac{C_{21}}{b} - \frac{C_{22}}{0.8b}\right)h_1 + 57.3\left(\frac{G_{21}}{b} - \frac{G_{22}}{0.8b}\right)\left(\frac{1}{\omega}\right)\dot{h}_1 + 57.3\frac{C_{22}}{0.8b}h_2 + 57.3\left(\frac{G_{22}}{0.8b}\right)\left(\frac{1}{\omega}\right)\dot{h}_2 \tag{B2}$$

where δ and β in radians have been converted to $\hat{\delta}$ and $\hat{\beta}$ in degrees. Before equations (B1) and (B2) were programed on the analog computer, they were amplitude

scaled. Amplitude scaling associates physical variables with computer voltages so that a full-scale physical variable produces a full-scale output voltage on the computer. Table VII shows the physical variable, the scale factor associating each physical variable with computer voltage, and the scaled variable. The maximum output voltage of the computer amplifiers was ±10 volts. The accelerations $\ddot{h}_1$ and $\ddot{h}_2$ were scaled because accelerometers were used to sense wing motion. Three assumptions were made in computing the scale factors in table VII. The assumptions are as follows:

(1) The acceleration, velocity, and displacement were sinusoidal.

(2) The maximum response amplitude occurred at the flutter frequency.

(3) The lowest frequency of interest was 4 Hz and the highest frequency was 25 Hz.

TABLE VII.- CONTROL LAW COMPUTER SCALING DATA

Physical variable	Maximum value of physical variable	Scale factor	Scaled variable
$\ddot{h}_1$	200.00 m/s^2	$50 \times 10^{-3} \frac{\text{volt}}{\text{m/s}^2}$	$\left[50 \times 10^{-3} \ddot{h}_1\right]$
$\ddot{h}_2$	200.00 m/s^2	$50 \times 10^{-3} \frac{\text{volt}}{\text{m/s}^2}$	$\left[50 \times 10^{-3} \ddot{h}_2\right]$
$\dot{h}_1$	2.50 m/s	$4.0 \frac{\text{volt}}{\text{m/s}}$	$\left[4.0 \dot{h}_1\right]$
$\dot{h}_2$	2.50 m/s	$4.0 \frac{\text{volt}}{\text{m/s}}$	$\left[4.0 \dot{h}_2\right]$
h_1	0.05 m	$200 \frac{\text{volt}}{\text{m}}$	$\left[200 h_1\right]$
h_2	0.05 m	$200 \frac{\text{volt}}{\text{m}}$	$\left[200 h_2\right]$
$\hat{\beta}$	10.00 deg	$1.0 \frac{\text{volt}}{\text{deg}}$	$\left[1.0 \hat{\beta}\right]$
$\hat{\delta}$	10.00 deg	$1.0 \frac{\text{volt}}{\text{deg}}$	$\left[1.0 \hat{\delta}\right]$
τ	0.25 s	$40.0 \frac{\text{volt}}{\text{s}}$	$\left[40.0 \tau\right]$

APPENDIX B

The term $1/\omega$ in equations (B1) and (B2) is particularly interesting and requires special attention. Instead of measuring frequency, multiplying by 2π, and inverting to form the $1/\omega$ term, the period τ was measured. The product $\tau\dot{h}$ was formed by using an electronic multiplier. The multiplier output is xy/10 for x and y inputs. If the scaled variables for τ, $[40\tau]$, and $\dot{h}$, $[4.0\dot{h}]$, from table VII are inserted in the multiplier equation, two computer-generated scaled variables are obtained:

$$\frac{[40\tau]\left[4.0\dot{h}_1\right]}{10} = \left[16\tau\dot{h}_1\right]$$

$$\frac{[4.0\tau]\left[4.0\dot{h}_2\right]}{10} = \left[16\tau\dot{h}_2\right]$$

Inserting the scaled variables from table VII and the computer-generated scaled variables into equations (B1) and (B2) and remembering that the scaled and unscaled equations must numerically remain the same, the following equations are obtained:

$$[1.0\hat{\beta}] = 57.3\,\frac{G_{12}}{(0.8b)(2\pi)(16)}\left[16\tau\dot{h}_2\right] - 57.3\,\frac{G_{12}}{(0.8b)(2\pi)(16)}\left[16\tau\dot{h}_1\right] \tag{B3}$$

$$[1.0\hat{\delta}] = \frac{57.3}{200}\left(\frac{C_{21}}{b} - \frac{C_{22}}{0.8b}\right)\left[200h_1\right] + \frac{57.3}{(2\pi)(16)}\left(\frac{G_{21}}{b} - \frac{G_{22}}{0.8b}\right)\left[16\tau\dot{h}_1\right] + \frac{57.3}{200}\,\frac{C_{22}}{0.8b}\left[200h_2\right]$$

$$+ \frac{57.3}{(2\pi)(16)}\,\frac{G_{22}}{0.8b}\left[16\tau\dot{h}_2\right] \tag{B4}$$

Equations (B3) and (B4) are the scaled equations which were programed on the analog computer. A block diagram of the computer circuit used to implement these equations is shown in figure 30. The scaled variables $\left[200h_1\right]$ and $\left[200h_2\right]$ are obtained by integrating the scaled accleration twice. The varibles $\left[16\tau\dot{h}_1\right]$ and $\left[16\tau\dot{h}_2\right]$ are formed by integrating the accelerations to obtain velocities and multiplying the velocities by the output of the period measuring circuit $[40\tau]$. The scaled variables are inputs to summing amplifiers with the gain for each input set to the value of its coefficient in equations (B3) and (B4). The outputs of the summing amplifiers are the inputs to the actuator loops. The most important and the most difficult parts of the control law to implement were the double integration to obtain displacements and the measurement of the period of oscillation. Therefore, the integrator circuit and the period measurement circuit are discussed.

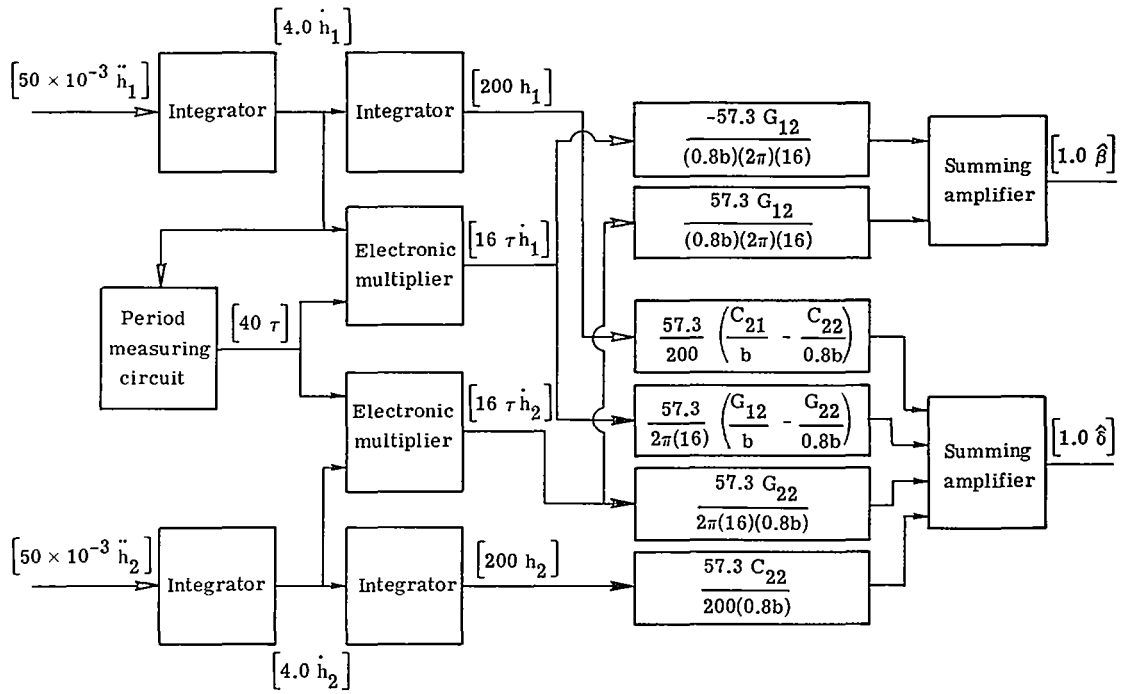

Figure 30.- Block diagram of the control law computer circuit.

Integrator circuit.- The goal in designing the control law feedbacks was to obtain a system which accurately represented the control law equations over the frequency range of 4 Hz to 25 Hz. Therefore, the amplitude error introduced by the integrators had to be small and also, the phase shift had to be as close as possible to -90° over the frequency range. Direct current integrators were rejected because any voltage offset or drift would be integrated continuously until the integrator output was saturated. The integrators selected are represented by the equation

$$\frac{E_O}{E_{IN}} = \frac{80s}{s^2 + 2s + 1}$$

where E_{IN} is the integrator input voltage; E_O is the integrator output voltage; and s is the Laplace transform variable. In order to satisfy the phase requirement, the break frequency for the second-order denominator was set at 1 rad/s. Critical damping was chosen for the second-order term to prevent output oscillations for transient inputs. The critical damping is very important when the two integrators are put in series to obtain displacement because the gain at 1 rad/s for two integrators is 1600, which means that in an underdamped integrator very small transient inputs would cause large output oscillations. Even with critical damping, nonoscillatory output transients will occur for very small transient inputs. To minimize these transients, the accelerometers used in this system were chosen carefully. Miniature oil-damped accelerometers were used. The

zero in the numerator of the integrator equation prevented static inputs from being transmitted to the output.

Period measurement circuit.- A block diagram of the period measurement circuit is shown in figure 31. The input to the circuit is the scaled velocity $\left[4.0\dot{h}_1\right]$. The input signal is converted to a square wave that is integrated with time to obtain a triangular wave. The peak value of the triangular wave is proportional to the period of the input signal. When the triangular wave is rectified, a new triangular wave with two peaks per cycle of the input signal is obtained. Sampling the rectified wave at the peaks produces a voltage output from the sample hold circuit proportional to the period of the input signal. The low pass filter smooths the output of the sample hold circuit to provide a continuous output signal. The period measurement circuit will provide an accurate measurement of the period of the input signal for single frequency periodic inputs only. This was not, however, a severe restriction because near flutter, the input signal is essentially a single frequency sinusoid. Additional information describing the period measurement circuit is presented in reference 25.

System integration.- The actuator loops were constructed by use of hard-wired electronics, whereas the control laws were programed on the analog computer. This arrangement proved to be very beneficial because for noncritical flutter conditions, the computer could be put into a standby configuration to allow changes in the control law programing without affecting operation of the actuator loops. The reliability of this system was very good with only a few minor problems occurring during many hours of laboratory and wind-tunnel testing.

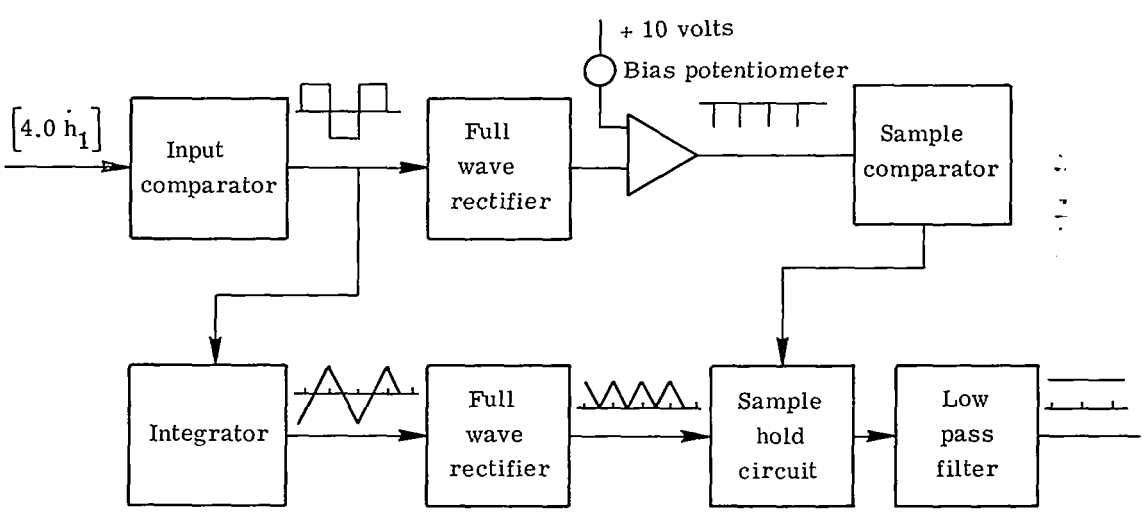

Figure 31.- Block diagram of period measuring circuit.

APPENDIX C

SUBCRITICAL RESPONSE (DAMPING) TECHNIQUES

The system performance was measured at subcritical test conditions (conditions below the flutter point) to evaluate the effectiveness of the flutter-suppression system. Three different methods were used to determine subcritical response of the delta-wing model. Each of these three methods is described briefly in this appendix.

Co-Quad Method

The Co-Quad method was originally proposed in reference 40 and later developed in more detail in reference 41. The method requires the application of a forced input to the model. A sinusoidal force of varying frequency is used to excite the model, and the resulting model dynamic response is measured. Special electronic equipment is used to resolve the model dynamic response into in-phase (called Co for coincident) and out-of-phase (called Quad for quadrature) components which are phase related to the sinusoidal force input signal. Figure 32 is a block diagram showing how the entire system functions. The forced input $\delta_{t,c}$ to the model and the output response $\ddot{h}_1$ from the model are routed to the special electronic equipment which, in turn, produces a normalized transfer ratio signal that is resolved into coincidence and quadrature components. Schematic representation of the variation of the coincidence and quadrature components with excitation frequency are included in figure 32. Damping is obtained for the wing mode of interest from the coincidence components. For example, by defining the frequency of the peak f_B and frequency of the notch f_A of the coincidence component, the damping is determined by using the equation shown in figure 32.

Randomdec Method

The Randomdec method is based on the procedure described in reference 42. This method does not require a sinusoidal forced input to the model, but depends on flow turbulence to supply a random force input. The Randomdec method is illustrated schematically in figure 33. The model output response is assumed to be composed of three components – the response to a step, to an impulse, and to a stationary random force. The system response to a step force is obtained by an ensemble average of a number of time sweeps, since the response to an impulse and random force average to zero. Time averaging of the response signal was accomplished by using a small special-purpose computer. In the implementation here the different time segments were averaged sequentially. That is, the computer processed all the results for one time sample before beginning to collect the data for the next sample. The averaging process for each time sample was started when the output signal reached a predetermined level. The model response output signal was passed

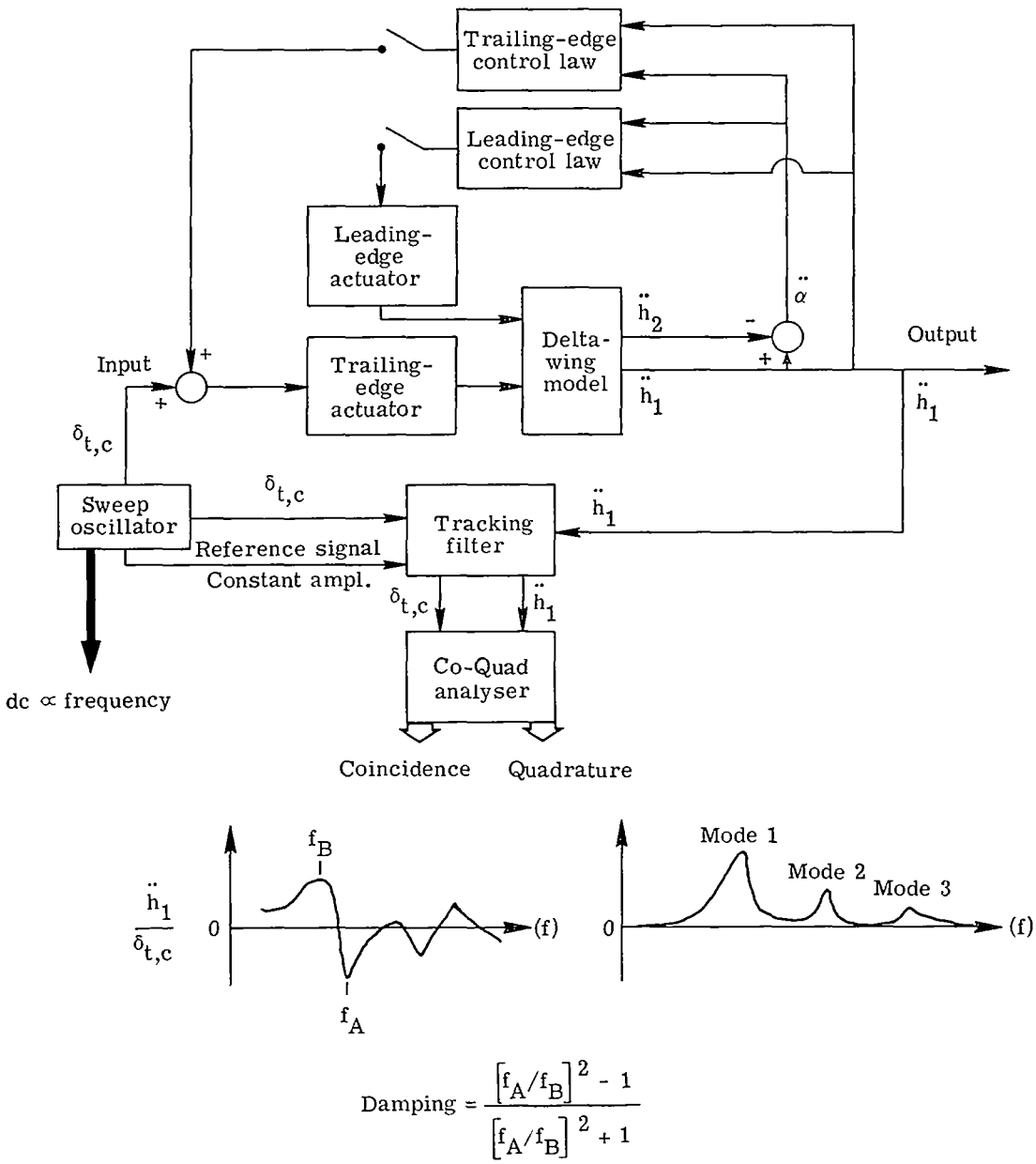

$$\text{Damping} = \frac{\left[f_A/f_B\right]^2 - 1}{\left[f_A/f_B\right]^2 + 1}$$

Figure 32.- Co-Quad subcritical response method.

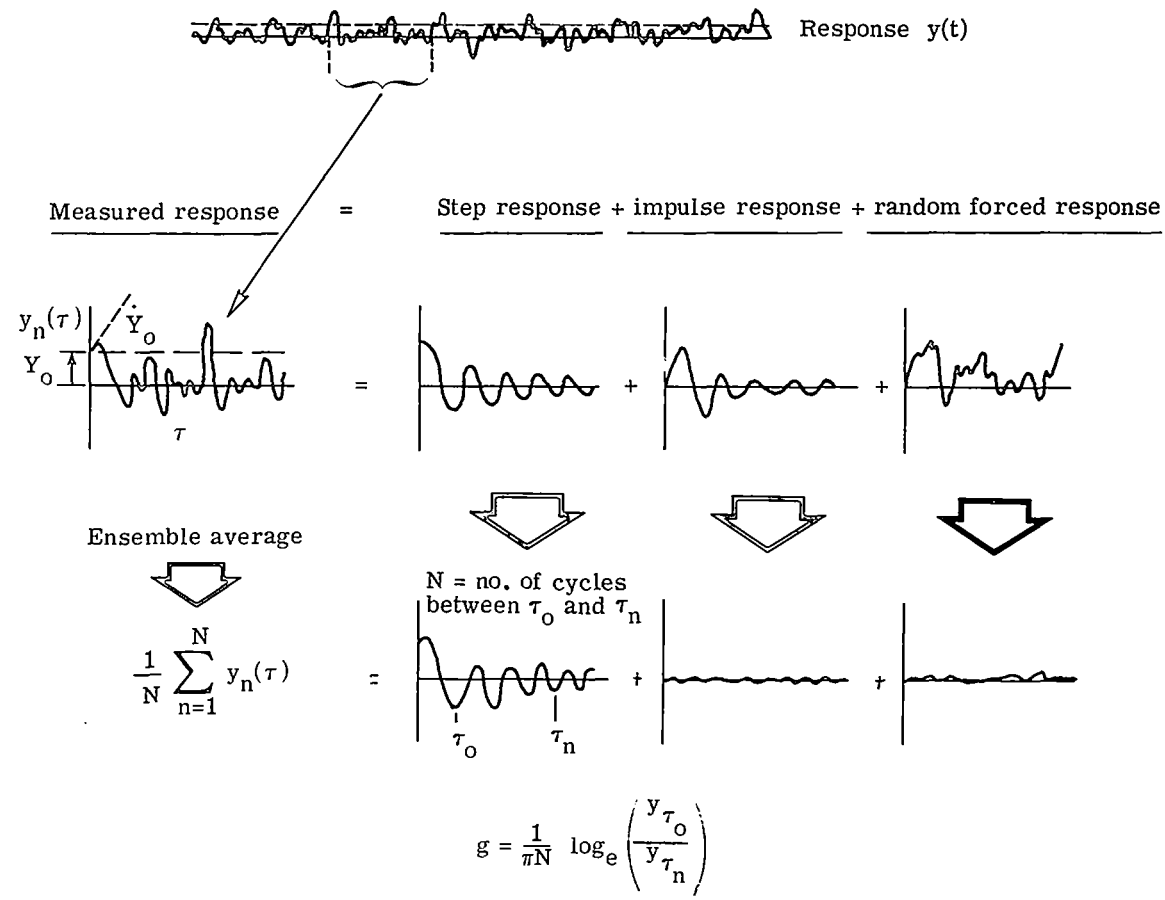

Figure 33.- Randomdec subcritical response method.

to a gating circuit. When the preset signal level was reached, the gate was opened, and the signal passed to the computer where it was averaged with values from previous samples. Electronic filters were used prior to the data sampling to isolate the frequencies of interest. The averaged signal has the appearance of the damped oscillation of a single-degree-of-freedom system. From this damped oscillatory signal the system damping is obtained by use of the logarithmic decrement formula.

Peak-Hold Spectrum Method

The Peak-Hold Spectrum method is similar to the method suggested in reference 37. The method is applicable to either sinusoidal forced or random excitation of the model. This study found by direct experimental comparison that applications to sinusoidal forced excitation produced higher quality data than did applications using random excitation. However, it should be noted that even with random excitation data the Peak-Hold Spectrum method gave flutter point prediction results comparable with the Co-Quad and Randomdec methods shown in figure 19.

The method is illustrated schematically in figure 34. A variable-frequency sinusoidal force $\delta_{t,c}$ excites the wing model. The output acceleration response $\ddot{h}_1$ is fed into a spectrum analyzer using the peak-hold mode of operation. In the peak-hold mode of operation the system works by initially entering into the analyzer memory a single spectrum composed of 250 filter locations, or frequency windows. Subsequent spectrums are taken periodically, but data in memory are updated only in a positive direction. That is, the current data in memory for a particular filter location are changed only if the new spectrum data value for that filter location exceeds the current value. Since the peak-hold spectrum is continuously displayed on an oscilloscope, the process is stopped when it becomes obvious that the spectrum is not being changed. Unlike the Co-Quad and Random-dec methods the damping itself is not obtained by using this method; rather, the reciprocal of amplitude is used as the measure of system stability.

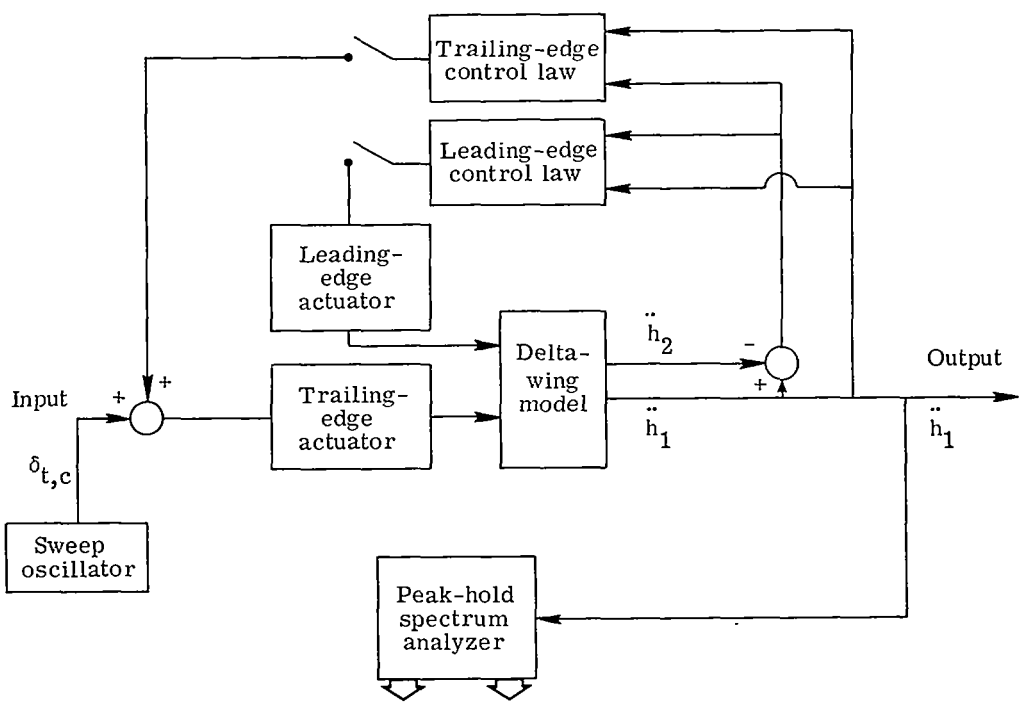

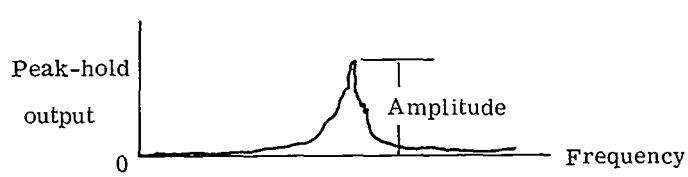

System stability ∝ inverse amplitude

Figure 34.- Peak-Hold Spectrum subcritical response method.

APPENDIX C

Plots of typical peak-hold output against frequency obtained from the delta-wing model test are shown in figure 35. Presented in the figure are open-loop and closed-loop results for three different dynamic pressures at a Mach number of 0.9.

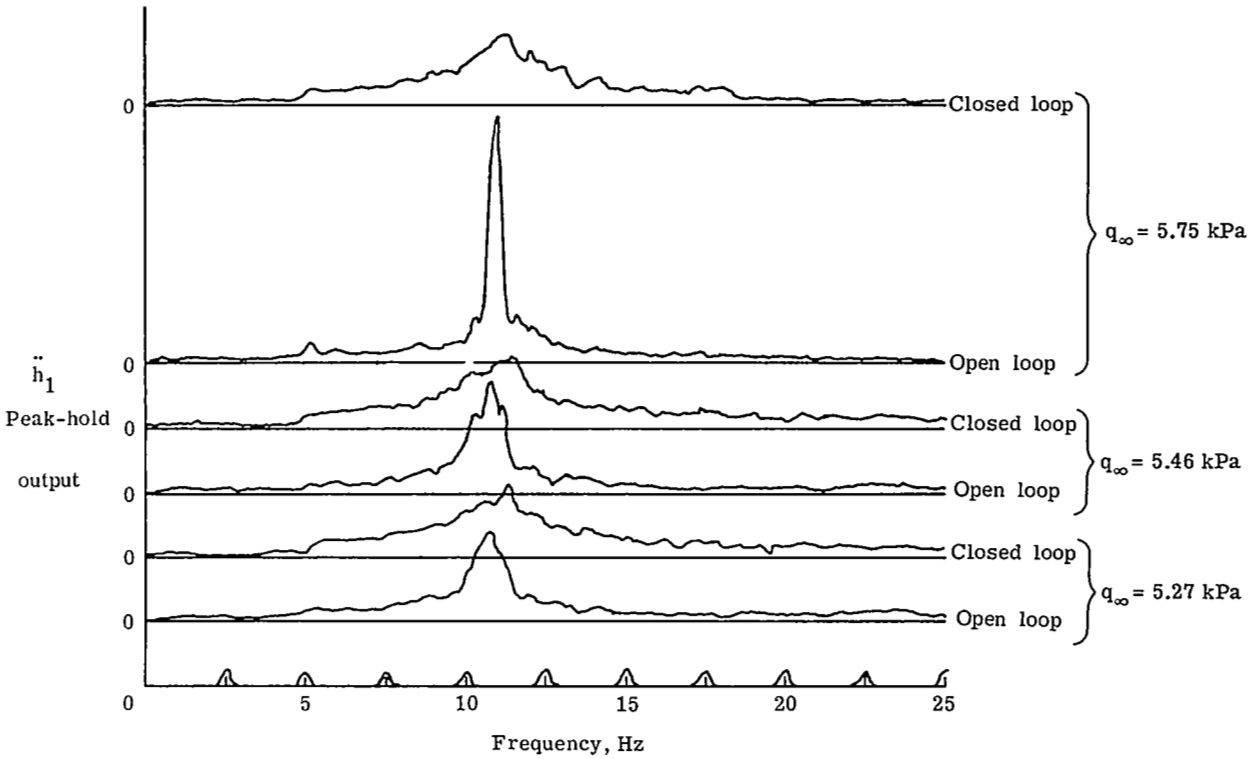

Figure 35.- Typical peak-hold spectrum results for delta-wing model.

REFERENCES

1. Garrick, I. E., ed.: Aerodynamic Flutter. Vol. V of AIAA Selected Reprint Series, Mar. 1969.

2. Pepping, R. A.: A Theoretical Investigation of the Oscillating Control Surface Frequency Response Technique of Flight Flutter Testing. J. Aeronaut. Sci., vol. 21, no. 8, Aug. 1954, pp. 533-542.

3. Bisplinghoff, Raymond L.; Ashley, Holt; and Halfman, Robert L.: Aeroelasticity. Addison-Wesley Pub. Co., Inc., c.1955.

4. Andrew, G. M.; and Johnson, J. M., Jr.: Automatic Control of Aeroelastic Modes. IAS Paper No. 62-86, June 1962.

5. Westerwick, R. A.: Multiple Sensors Feasibility Study. Volume II. ASD-TDR 63-378, Vol. II, U.S. Air Force, June 1963.

6. Davis, H. Max; and Swaim, Robert L.: Controlling Dynamic Response in Rough Air. AIAA Paper No. 66-997, Nov.-Dec. 1966.

7. Dempster, John B.; and Roger, Kenneth L.: Evaluation of B-52 Structural Response to Random Turbulence With Stability Augmentation Systems. J. Aircraft, vol. 4, no. 6, Nov.-Dec. 1967, pp. 507-512.

8. Wykes, John H.; and Mori, Alva S.: Techniques and Results of an Analytical Investigation Into Controlling the Structural Modes of Flexible Aircraft. AIAA Symposium on Structural Dynamics and Aeroelasticity, Aug.-Sept. 1965, pp. 419-433.

9. Dempster, John B.; and Arnold, James I.: Flight Test Evaluation of an Advanced Stability Augmentation System for the B-52 Aircraft. AIAA Paper No. 68-1068, Oct. 1968.

10. Wykes, John H.; and Kordes, Eldon E.: Analytical Design and Flight Tests of a Modal Suppression System on the XB-70 Airplane. Aeroelastic Effects From a Flight Mechanics Standpoint, AGARD CP-46, 1970, pp. 23-1 – 23-18.

11. Johannes, R. P.: Active Flutter Control – Flight Test System Synthesis. Paper No. 7-B1, 1971 Joint Automatic Control Conference (St. Louis, Mo.), Aug. 1971.

12. Topp, L. J.: Potential Performance Gains by Use of a Flutter Suppression System. Paper No. 7-B3, 1971 Joint Automatic Control Conference (St. Louis, Mo.), Aug. 1971.

13. Triplett, W. E.: A Feasibility Study of Active Wing/Store Flutter Control. Paper No. 7-B4, 1971 Joint Automatic Control Conference (St. Louis, Mo.), Aug. 1971.

14. Lyons, M. G.; Vepa, R.; McIntosh, S. C., Jr.; and DeBra, D. B.: Control Law Synthesis and Sensor Design for Active Flutter Suppression. AIAA Paper No. 73-832, Aug. 1973.

15. Buchek, Philip M.: Modern Control Techniques in Active Flutter Suppression Using a Control Moment Gyro. SUDAAR No. 474, Stanford Univ., Mar. 1974. (Available as NASA CR-138494.)

16. Nissim, E.: Flutter Suppression and Gust Alleviation Using Active Controls. TAE Rep. No. 198, Technion-Israel Inst. Technol., 1974. (Available as NASA CR-138658.)

17. Rainey, A. Gerald: Advanced Active Controls Technology. Vehicle Technology for Civil Aviation – The Seventies and Beyond, NASA SP-292, 1971, pp. 245-257.

18. Thompson, G. O.; and Kass, G. J.: Active Flutter Suppression – An Emerging Technology. Paper No. 7-B2, 1971 Joint Automatic Control Conference (St Louis, Mo.), Aug. 1971.

19. Hood, Ray V.: Active Controls Changing the Rules of Structural Design. Astronaut. & Aeron., vol. 10, no. 8, Aug. 1972, pp. 50-55.

20. Rainey, A. Gerald; Ruhlin, Charles L.; and Sandford, Maynard C.: Active Control of Aeroelastic Response. Stability and Control, AGARD CP-119, 1972, pp. 16-1 – 16-5.

21. Noll, Thomas E.; and Felt, Larry R.: Active Flutter Suppression – A Practical Application. Proceedings of National Aerospace Electronics Conference 1973, IEEE, May 1973, pp. 329-334.

22. Doggett, Robert V., Jr.; Abel, Irving; and Ruhlin, Charles L.: Some Experiences Using Wind-Tunnel Models in Active Control Studies. Advanced Control Technology and Its Potential for Future Transport Aircraft, NASA TM X-70240, 1974.

23. Pratt, Kermit G.: A Survey of Active Controls Benefits to Supersonic Transports. Advanced Control Technology and Its Potential for Future Transport Aircraft, NASA TM X-70240, 1974.

24. Nissim, E.: Flutter Suppression Using Active Controls Based on the Concept of Aerodynamic Energy. NASA TN D-6199, 1971.

25. Sevart, Frank D.: Analysis of Aeroelastic Model Stability Augmentation Systems. Doc. D3-8390-4, Boeing Co., Mar. 1971. (Available as NASA CR-132354.)

26. Sevart, F. D.; Patel, S. M.; and Wattman, W. J.: Analysis and Testing of Stability Augmentation Systems – Final Report. Doc. D3-8884, Boeing Co., June 1972. (Available as NASA CR-132349.)

27. Sevart, Francis D.; and Patel, Suresh M.: Analysis and Testing of Aeroelastic Model Stability Augmentation Systems – Final Report. Doc. D3-9245, Boeing Co., Oct. 1973. (Available as NASA CR-132345.)

28. Abel, Irving; and Sandford, Maynard C.: Status of Two Studies on Active Control of Aeroelastic Response. NASA TM X-2909, 1973.

29. Sandford, Maynard C.; Abel, Irving; and Gray, David L.: Transonic Study of Active Flutter Suppression Based on an Energy Concept. J. Aircraft, vol. 12, no. 2, Feb. 1975, pp. 72-77.

30. Hunt, Gerald L.; and Walberg, Gerald D.: Calculated Mode Shapes and Pressure Distributions at Flutter for a Highly Tapered Horizontal Tail in Subsonic Flow. NASA TN D-1008, 1962.

31. Sandford, Maynard C.; Ruhlin, Charles L.; and Abel, Irving: Transonic Flutter Study of a 50.5° Cropped-Delta Wing With Two Rearward-Mounted Nacelles. NASA TN D-7544, 1974.

32. Bergmann, Gerald E.; and Sevart, Francis D.: Design and Evaluation of Miniature Control Surface Actuation Systems for Aeroelastic Models. J. Aircraft, vol. 12, no. 3, Mar. 1975, pp. 129-134.

33. Naumann, Eugene C.; and Flagge, Bruce: A Noncontacting Displacement Measuring Technique and Its Application to Current Vibration Testing. Preprint No. 16.18-5-66, Instrum. Soc. America, Oct. 1966.

34. De Vries, G.: Sondage des Systèmes Vibrants par Masses Additionnelles. Rech. Aéronaut., no. 30, Nov.-Dec. 1952, pp. 47-49.

35. Abel, Irving: A Wind-Tunnel Evaluation of Analytical Techniques for Predicting Static Stability and Control Characteristics of Flexible Aircraft. NASA TN D-6656, 1972.

36. Yates, E. Carson, Jr.; Land, Norman S.; and Foughner, Jerome T.: Measured and Calculated Subsonic and Transonic Flutter Characteristics of a 45° Sweptback Wing Planform in Air and in Freon-12 in the Langley Transonic Dynamics Tunnel. NASA TN D-1616, 1963.

37. Houbolt, J. C.; and Rainey, A. G.: On the Prediction of Critical Flutter Conditions From Subcritical Response Data and Some Related Wind-Tunnel Experience. Proceedings of the 1958 Flight Flutter Testing Symposium, NASA SP-385, 1975, pp. 23-29.

38. Albano, Edward; and Rodden, William P.: A Doublet-Lattice Method for Calculating Lift Distributions on Oscillating Surfaces in Subsonic Flows. AIAA J., vol. 7, no. 2, Feb. 1969, pp. 279-285; Errata, vol. 7, no. 11, Nov. 1969, p. 2192.

39. Greville, T. N. E.: Spline Functions, Interpolation, and Numerical Quadrature. Mathematical Methods for Digital Computers, Vol. II. Anthony Ralston and Herbert S. Wilf, eds., John Wiley & Sons, Inc., c.1967, pp. 156-168.

40. Kennedy, Charles C.; and Pancu, C. D. P.: Use of Vectors in Vibration Measurement and Analysis. J. Aeronaut. Sci., vol. 14, no. 11, Nov. 1947, pp. 603-625.

41. Keller, Anton C.: Vector Component Techniques: A Modern Way To Measure Modes. Sound & Vib., vol. 3, no. 3, Mar. 1969, pp. 18-26.

42. Cole, Henry A., Jr.: On-line Failure Detection and Damping Measurement of Aerospace Structures by Random Decrement Signatures. NASA CR-2205, 1973.

NATIONAL AERONAUTICS AND SPACE ADMINISTRATION
WASHINGTON, D.C. 20546

OFFICIAL BUSINESS
PENALTY FOR PRIVATE USE $300

SPECIAL FOURTH-CLASS RATE BOOK

POSTAGE AND FEES PAID
NATIONAL AERONAUTICS AND SPACE ADMINISTRATION
451

U.S.MAIL

120 001 C1 U D 751204 S00903DS
DEPT OF THE AIR FORCE
AF WEAPONS LABORATORY
ATTN: TECHNICAL LIBRARY (SUL)
KIRTLAND AFB NM 87117

POSTMASTER: If Undeliverable (Section 158 Postal Manual) Do Not Return

"The aeronautical and space activities of the United States shall be conducted so as to contribute . . . to the expansion of human knowledge of phenomena in the atmosphere and space. The Administration shall provide for the widest practicable and appropriate dissemination of information concerning its activities and the results thereof."

—NATIONAL AERONAUTICS AND SPACE ACT OF 1958

NASA SCIENTIFIC AND TECHNICAL PUBLICATIONS

TECHNICAL REPORTS: Scientific and technical information considered important, complete, and a lasting contribution to existing knowledge.

TECHNICAL NOTES: Information less broad in scope but nevertheless of importance as a contribution to existing knowledge.

TECHNICAL MEMORANDUMS: Information receiving limited distribution because of preliminary data, security classification, or other reasons. Also includes conference proceedings with either limited or unlimited distribution.

CONTRACTOR REPORTS: Scientific and technical information generated under a NASA contract or grant and considered an important contribution to existing knowledge.

TECHNICAL TRANSLATIONS: Information published in a foreign language considered to merit NASA distribution in English.

SPECIAL PUBLICATIONS: Information derived from or of value to NASA activities. Publications include final reports of major projects, monographs, data compilations, handbooks, sourcebooks, and special bibliographies.

TECHNOLOGY UTILIZATION PUBLICATIONS: Information on technology used by NASA that may be of particular interest in commercial and other non-aerospace applications. Publications include Tech Briefs, Technology Utilization Reports and Technology Surveys.

Details on the availability of these publications may be obtained from:

SCIENTIFIC AND TECHNICAL INFORMATION OFFICE

NATIONAL AERONAUTICS AND SPACE ADMINISTRATION

Washington, D.C. 20546